Monthly Notices of the ROYAL ASTRONOMICAL SOCIETY

MNRAS **527,** 9343–9358 (2024) https://doi.org/10.1093/mnras/stad3675
Advance Access publication 2023 November 28

WISDOM project – XVIII. Molecular gas distributions and kinematics of three megamaser galaxies

Fu-Heng Liang (梁赋珩) [1]★ Mark D. Smith [1] Martin Bureau,[1,2]★ Feng Gao,[3] Timothy A. Davis [4] Michele Cappellari [1] Jacob S. Elford [4] Jenny E. Greene,[5] Satoru Iguchi [6,7] Federico Lelli [8] Anan Lu [9] Ilaria Ruffa [4] Thomas G. Williams [1] and Hengyue Zhang [1]

[1]*Sub-department of Astrophysics, Department of Physics, University of Oxford, Denys Wilkinson Building, Keble Road, Oxford, OX1 3RH, UK*
[2]*Yonsei Frontier Lab and Department of Astronomy, Yonsei University, 50 Yonsei-ro, Seodaemun-gu, Seoul 03722, Republic of Korea*
[3]*Hamburger Sternwarte, Universität Hamburg, Gojenbergsweg 112, D-21029, Hamburg, Germany*
[4]*Cardiff Hub for Astrophysics Research & Technology, School of Physics & Astronomy, Cardiff University, Queens Buildings, Cardiff, CF24 3AA, UK*
[5]*Department of Astrophysical Sciences, Princeton University, Princeton, NJ 08544, USA*
[6]*Department of Astronomical Science, SOKENDAI (The Graduate University of Advanced Studies), Mitaka, Tokyo 181-8588, Japan*
[7]*National Astronomical Observatory of Japan, National Institutes of Natural Sciences, Mitaka, Tokyo 181-8588, Japan*
[8]*INAF, Arcetri Astrophysical Observatory, Largo Enrico Fermi 5, I-50125 Florence, Italy*
[9]*Trottier Space Institute and Department of Physics, McGill University, 3600 University Street, Montreal, QC H3A 2T8, Canada*

Accepted 2023 November 23. Received 2023 November 23; in original form 2023 July 20

ABSTRACT

The co-evolution of galaxies and supermassive black holes (SMBHs) underpins our understanding of galaxy evolution, but different methods to measure SMBH masses have only infrequently been cross-checked. We attempt to identify targets to cross-check two of the most accurate methods, megamaser, and cold molecular gas dynamics. Three promising galaxies are selected from all those with existing megamaser SMBH mass measurements. We present Atacama Large Millimeter/sub-millimeter Array (ALMA) ^{12}CO (2–1) and 230-GHz continuum observations with angular resolutions of $\approx 0\farcs5$. Every galaxy has an extended rotating molecular gas disc and 230-GHz continuum source(s), but all also have irregularities and/or non-axisymmetric features: NGC 1194 is highly inclined and has disturbed and lopsided central ^{12}CO (2–1) emission; NGC 3393 has a nuclear disc with fairly regular but patchy ^{12}CO (2–1) emission with little gas near the kinematic major axis, faint emission in the very centre, and two brighter structures reminiscent of a nuclear ring and/or spiral; NGC 5765B has a strong bar and very bright ^{12}CO (2–1) emission concentrated along two bisymmetric offset dust lanes and two bisymmetric nuclear spiral arms. ^{12}CO (2–1) and ^{12}CO (3–2) observations with the James Clerk Maxwell Telescope are compared with the ALMA observations. Because of the disturbed gas kinematics and the impractically long integration times required for higher angular resolution observations, none of the three galaxies is suitable for a future SMBH mass measurement. None the less, increasing the number of molecular gas observations of megamaser galaxies is valuable, and the ubiquitous disturbances suggest a link between large-scale gas properties and the existence of megamasers.

Key words: masers – galaxies: individual: NGC 1194, NGC 3393, NGC 5765B – galaxies: ISM – galaxies: kinematics and dynamics – galaxies: nuclei.

1 INTRODUCTION

Over the past few decades, tight empirical scaling relations have suggested that supermassive black holes (SMBHs) in galaxy centres co-evolve with their host galaxies across cosmic time (see e.g. Kormendy & Ho 2013; D'Onofrio, Marziani & Chiosi 2021 for reviews). The tightest correlation is between SMBH mass and stellar velocity dispersion ($M_{\rm BH}$–$\sigma_\star$ relation; e.g. Ferrarese & Merritt 2000; Gebhardt et al. 2000; Beifiori et al. 2012; van den Bosch 2016). Numerous studies have probed potential SMBH and host galaxy self-regulating growth mechanisms through feedback from active galactic nuclei (AGN; see e.g. Alexander & Hickox 2012 for a review). Understanding SMBH properties (mass, growth history, feedback, etc.) is thus critical to our understanding of galaxy evolution.

These scaling relations are however built from no more than ≈160 SMBHs with reliable direct (i.e. dynamical) mass measurements. Moreover, these come from a variety of measurement methods such as stellar dynamics, ionized-gas dynamics, megamaser (hereafter 'maser' for short) dynamics and more recently cold molecular gas dynamics, each with different limitations and potential biases. In particular, most methods are only applicable to certain galaxy types,

★ E-mail: ericfuhengliang@gmail.com (FHL); martin.bureau@physics.ox.ac.uk (MB)

so that only a few of the measurements have been cross-checked (see Walsh et al. 2013 for an earlier summary). These include: (i) 'stars versus ionized gas' in IC 1459 (Cappellari et al. 2002), NGC 3379 (Shapiro et al. 2006), Centaurus A (Neumayer et al. 2007; Cappellari et al. 2009), NGC 3998 (Walsh et al. 2012), NGC 4335 (Verdoes Kleijn et al. 2002) and M81 (Devereux et al. 2003); (ii) 'stars versus ionized gas versus direct imaging' in M87 (Gebhardt & Thomas 2009; Gebhardt et al. 2011; Walsh et al. 2013; Event Horizon Telescope Collaboration et al. 2019; Jeter, Broderick & McNamara 2019; Jeter & Broderick 2021; Broderick et al. 2022; Liepold, Ma & Walsh 2023; Simon, Cappellari & Hartke 2024); (iii) 'stars versus ionized gas versus reverberation mapping' in NGC 3227 and NGC 4151 (Davies et al. 2006; Onken et al. 2007; Hicks & Malkan 2008); (iv) 'stars versus masers' in NGC 4258 (Siopis et al. 2009; Drehmer et al. 2015); (v) 'ionized gas versus masers' in NGC 4258 (Pastorini et al. 2007); and (vi) 'stars versus proper motions' in the Milky Way (Sagittarius A∗; Feldmeier-Krause et al. 2017). Many of these cross-checking attempts were however affected by disturbed ionized-gas kinematics and/or other issues, and thus were not particularly decisive.

Across these methods, maser dynamics is generally regarded as providing the most accurate and precise SMBH mass measurements, as it measures, with high accuracy, the gas kinematics close to the SMBHs, yielding a typical mass uncertainty of $\lesssim$10 per cent dominated by the galaxy distance (e.g. Herrnstein et al. 2005). This method spatially resolves the Keplerian rotation of the parsec-scale discs in which the masers are located, within the spheres of influence (SoIs) of the SMBHs. Maser galaxies are however, rare, requiring edge-on masing discs and thus a particular type of nuclear activity mostly present in late-type disc galaxies (i.e. a Seyfert 2 AGN), with a narrow range of SMBH masses ($\sim 10^7$ M$_\odot$). None the less, maser measurements offer valuable benchmarks for cross-checks (and potentially cross-calibration) with other methods, as stressed in many works (e.g. van den Bosch et al. 2016). However, maser SMBH mass measurements seem to systematically lie below (i.e. at smaller SMBH masses than) the $M_{\rm BH}$–$\sigma_\star$ relation, even when controlling for morphological type (e.g. Greene et al. 2016), and therefore may not follow the general trend defined by all other measurements. This may reveal intrinsic scatter in the $M_{\rm BH}$–$\sigma_\star$ relation, but it may also arise from systematic effects across the different methods. Cross-checks of individual SMBH measurements is thus imperative.

Due to the high angular resolutions afforded by current mm/submm interferometers, cold molecular gas (particularly CO) dynamics has recently been used to weigh SMBHs. Following the first measurement in NGC 4526 (Davis et al. 2013), new measurements mostly using the exquisite sensitivity and angular resolution of the Atacama Large Millmeter/sub-millimeter Array (ALMA) have been made by the millimetre-Wave Interferometric Survey of Dark Object Masses (WISDOM; Davis et al. 2017; Onishi et al. 2017; Davis et al. 2018; North et al. 2019; Smith et al. 2019; Davis et al. 2020; Smith et al. 2021; Lelli et al. 2022; Ruffa et al. 2023) and others (e.g. Onishi et al. 2015; Barth et al. 2016; Boizelle et al. 2019; Nagai et al. 2019; Ruffa et al. 2019b; Nguyen et al. 2020; Boizelle et al. 2021; Cohn et al. 2021; Nguyen et al. 2021; Kabasares et al. 2022; Nguyen et al. 2022). Many of these observations probe CO emission on the same spatial scales as those probed by masers, and the latest in fact does better (Zhang et al., in preparation). This method has only weak biases toward particular galaxy types and is conceptually very simple, mainly constrained by the size of each SMBH SoI and the existence of a central regularly rotating molecular gas disc. Given its increasing popularity, cross-checking CO and maser (as well as other methods) SMBH dynamical measurements is highly desirable.

This paper thus aims to identify promising targets for future CO SMBH mass measurements (utilising higher resolution follow-up observations), from galaxies with existing maser measurements. Simultaneously, this paper reveals the molecular gas properties of several maser host galaxies at $\sim$100 pc scale, essential to probe the cold interstellar medium (ISM) conditions required for masing. In Section 2, we present a compilation of existing maser SMBH mass measurements and the three targets selected here for further study. In Section 3, we describe new intermediate-resolution ALMA as well as James Clerk Maxwell Telescope (JCMT) observations of the molecular gas and mm-continuum emission of those three galaxies, along with standard data products. The potential for SMBH mass measurements using CO observations at higher angular resolutions is discussed in Section 4. We discuss the link between molecular gas disc properties and maser emission with an enlarged sample in Section 5. Finally, we summarize and conclude in Section 6.

2 TARGETS

2.1 Candidate selection

To cross-check cold molecular gas and maser dynamical SMBH mass measurements, we must first identify galaxies with existing maser measurements that also appear promising for molecular gas measurements. We use the compilation of SMBH mass measurements of van den Bosch (2016) as our starting point, including all maser measurements in their Tables 2 and 3. We update the galaxy distances when better determinations are now available, including those from maser monitoring programmes (NGC 6264, NGC 6323, NGC 5765B, and UGC 3789), part of the Megamaser Cosmology Project (MCP; see Braatz et al. 2009 and Table 1), and adjust the SMBH masses accordingly ($M_{\rm BH} \propto D$ for all dynamical mass measurements, where D is the galaxy distance). We remove NGC 1386, as there is no refereed source for its SMBH mass and its ^{12}CO (1–0)[1] has already been imaged with ALMA by Ramakrishnan et al. (2019) and Zabel et al. (2019). We also correct the SMBH mass of IC 2560 quoted in van den Bosch (2016; $\log(M_{\rm BH}/{\rm M}_\odot) = 7.64 \pm 0.05$) back to the original mass reported by Yamauchi et al. (2012; $\log(M_{\rm BH}/{\rm M}_\odot) = 6.54 \pm 0.06$). This megamaser parent sample is summarized in Table 1.

We then apply the following selection criteria to retain the best cold molecular gas measurement candidates. Whether each galaxy fulfils each criterion is listed in Table 1.

(i) SMBH SoI angular radius $\theta_{\rm SoI} \equiv R_{\rm SoI}/D > 0\farcs01$, where the SMBH SoI physical radius $R_{\rm SoI} \equiv {\rm G}M_{\rm BH}/\sigma_\star^2$, so that the SoI can be spatially resolved using ALMA's longest baselines at CO (2–1) (band 6).

(ii) *Hubble Space Telescope* (*HST*) imaging (available for all galaxies) showing a regular central dust disc, suggesting a central molecular gas disc in ordered rotation.

[1]Hereafter, we omit the carbon atomic mass number and refer to the ^{12}CO isotope simply as CO.

Table 1. Predicted SMBH SoIs and selection criteria of maser galaxies.

Galaxy	Distance (Mpc)	$\log(M_{\rm BH}/{\rm M}_\odot)$	$\sigma_\star$ (km s^{-1})	$R_{\rm SoI}$ (pc)	$\theta_{\rm SoI}$ (mas)	SoI	Dust	Dec.	References
(1)	(2)	(3)	(4)	(5)	(6)	(7)	(8)	(9)	(10)
Circinus	2.8 ± 0.5	6.06 ± 0.07	158 ± 18	0.20 ± 0.06	15 ± 5	✓	✓	✓	(1)
ESO 558–009	108 ± 6	7.23 ± 0.03	170 ± 20	2.5 ± 0.6	4.9 ± 1.2	-	✓	✓	(2)
IC 1481	79 ± 6	7.11 ± 0.13	95 ± 27	6.1 ± 3.9	16 ± 10	✓	–	✓	(3)
IC 2560	31 ± 13	6.54 ± 0.06	141 ± 10	0.90 ± 0.18	6.0 ± 2.8	–	–	✓	(4)
J0437 + 2456	65 ± 4	6.46 ± 0.05	110 ± 13	1.03 ± 0.27	3.3 ± 0.9	–	–	–	(2)
Mrk1029	121 ± 7	6.28 ± 0.12	132 ± 15	0.47 ± 0.17	0.8 ± 0.3	–	–	✓	(2)
NGC 1068	16 ± 9	6.95 ± 0.02	151 ± 7	1.67 ± 0.17	22 ± 13	✓	–	✓	(5)
NGC 1194	58 ± 6	7.85 ± 0.02	148 ± 24	14 ± 5	50 ± 17	✓	✓	✓	(6)
NGC 1320	34.2 ± 1.9	6.74 ± 0.21	141 ± 16	1.2 ± 0.7	7 ± 4	–	–	✓	(2)
NGC 2273	29.5 ± 1.9	6.93 ± 0.02	145 ± 17	1.8 ± 0.4	12.3 ± 3.0	✓	✓	–	(6)
NGC 2960	67 ± 7	7.03 ± 0.02	151 ± 7	2.01 ± 0.21	6.2 ± 0.9	–	✓	✓	(6)
NGC 3079	15.9 ± 1.2	6.36 ± 0.09	145 ± 7	0.47 ± 0.11	6.1 ± 1.5	–	✓	–	(7)
NGC 3393	49 ± 8	7.3 ± 0.4	148 ± 10	3.6 ± 2.5	15 ± 11	✓	✓	✓	(3), (8)
NGC 4258	7.3 ± 0.5	7.58 ± 0.03	115 ± 11	12.4 ± 2.4	351 ± 73	✓	–	–	(9), (10)
NGC 4388	16.5 ± 1.6	6.86 ± 0.01	107 ± 7	2.7 ± 0.4	34 ± 6	✓	–	✓	(6)
NGC 4945	3.58 ± 0.22	6.13 ± 0.18	135 ± 6	0.32 ± 0.14	18 ± 8	✓	–	✓	(10), (11)
NGC 5495	96 ± 5	7.04 ± 0.08	166 ± 19	1.7 ± 0.5	3.7 ± 1.1	–	–	✓	(2)
NGC 5765B	112 ± 5	7.61 ± 0.04	158 ± 18	7.0 ± 1.7	13 ± 3	✓	✓	✓	(12)
NGC 6264	144 ± 19	7.49 ± 0.06	158 ± 15	5.3 ± 1.2	7.6 ± 2.0	–	✓	–	(13)
NGC 6323	107 ± 36	6.97 ± 0.14	158 ± 26	1.6 ± 0.7	3.1 ± 1.7	–	–	–	(14)
UGC 3789	50 ± 5	7.06 ± 0.05	107 ± 12	4.3 ± 1.1	18 ± 5	✓	–	–	(15)
UGC 6093	152 ± 15	7.41 ± 0.03	155 ± 18	4.6 ± 1.1	6.3 ± 1.6	–	–	✓	(16)

Notes. Column 1: galaxy name. Column 2: distance. Column 3: maser-derived SMBH mass. Column 4: stellar velocity dispersion measured within one effective radius, using a variety of methods (van den Bosch 2016). Columns 5 and 6: SMBH SoI physical radius and angular radius. Columns 7–9: selection criterion fulfillment. Column 10: maser SMBH mass measurement references: (1) Greenhill et al. (2003), (2) Gao et al. (2017), (3) Huré et al. (2011), (4) Yamauchi et al. (2012), (5) Lodato & Bertin (2003), (6) Kuo et al. (2011), (7) Yamauchi et al. (2004), (8) Kondratko, Greenhill & Moran (2008), (9) Herrnstein et al. (2005), (10) Kormendy & Ho (2013), (11) Greenhill, Moran & Herrnstein (1997), (12) Gao et al. (2016), (13) Kuo et al. (2013), (14) Kuo et al. (2015), (15) Reid et al. (2013) and (16) Zhao et al. (2018). We note that the maser emission in some galaxies may be dominated or contaminated by non-disc maser sources, such as masers in outflows/jets; see Pesce et al. (2015) for a clean subset with pure disc-maser galaxies and Keplerian rotation.

(iii) Declination $-66^\circ < \delta < +20^\circ$, to ensure a fairly round ALMA synthesized beam and minimize shadowing.[2]

The only galaxies to satisfy all these requirements are Circinus, NGC 1194, NGC 3393, and NGC 5765B. Cold molecular gas in Circinus has already been observed with ALMA at high angular resolution ($\approx 0\farcs2$) and it is reported to have a disturbed velocity field (Izumi et al. 2018; Tristram et al. 2022). This galaxy is therefore not suited to cold gas dynamical modelling to derive a SMBH mass, and it is not considered further in this paper. The basic properties of the other three galaxies, for which we obtained and present new ALMA data here, are listed in Table 2. We also discuss each galaxy in more details below.

2.2 NGC 1194

NGC 1194 is a lenticular galaxy harbouring a Seyfert 2 AGN (Oh et al. 2018), for which we adopt a distance $D = 58 \pm 6$ Mpc. This distance was estimated from NGC 1194's Local Group-centric redshift (Karachentsev & Makarov 1996) by Kormendy & Ho (2013) and Saglia et al. (2016) assuming a cosmology derived from the *Wilkinson Microwave Anisotropy Probe* (*WMAP*) 5-year data (Komatsu et al. 2009). NGC 1194 was first reported to harbour H_2O megamasers by Greenhill, Tilak & Madejski (2008) and is part of the MCP. It has a relatively large maser disc with an inner radius of 0.51 pc and an outer radius of 1.33 pc. It hosts the most massive SMBH derived using the maser method to date, $M_{\rm BH} = (7.1 \pm 0.3) \times 10^7$ M$_\odot$ at our adopted distance above (Kuo et al. 2011). The maser disc has an inclination $i \approx 85^\circ$ with a kinematic position angle[3] $PA_{\rm kin} = 337^\circ$, while the galaxy's overall inclination is $\approx 50^\circ$ with a morphological position angle $PA_{\rm mor} = 145^\circ$, as determined from an *r*-band image from the Sloan Digital Sky Survey (SDSS; Adelman-McCarthy et al. 2008). No warp is detected in the maser disc.

Previous studies have reported atomic hydrogen out to a galactocentric radius of $\approx 120''$ (≈ 4 kpc; Sun et al. 2013) and patchy warm molecular hydrogen on a scale of $1\farcs6$ (450 pc), limited by the telescope field of view (FoV; Greene et al. 2014). Ionized gas has been detected through *K*-band emission lines (e.g. Brγ, [Si VI], and [Ca VIII]) at the galaxy centre by Greene et al. (2014) and through the [O III] optical emission line over a slightly more extended region (700×470 pc^2; Schmitt et al. 2003). Koss et al. (2021) did not detect cold molecular gas using the Atacama Pathfinder Experiment, with a CO (2–1) 3σ upper limit of 2×10^7 K km s^{-1} pc^2 (9 Jy km s^{-1}), consistent with (i.e. larger than) our detected flux reported in Section 3.3.1.

[2]We note that even if we relax this criterion to $-90^\circ \leqq \delta \leqq +47^\circ$, to reach the absolute declination limit of ALMA, the final sample of galaxies meeting all of our selection criteria does not change.

[3]The kinematic (morphological) position angle is measured from north through east until the largest receding velocity (photometric major axis) is reached.

2.3 NGC 3393

NGC 3393 is an SBa galaxy (de Vaucouleurs et al. 1991) at an adopted distance $D = 49 \pm 8$ Mpc. This distance was again estimated from the Local Group-centric redshift (Karachentsev & Makarov 1996) by Kormendy & Ho (2013) and Saglia et al. (2016), assuming the cosmology derived from *WMAP* 5-year data (Komatsu et al. 2009). NGC 3393 has a large-scale stellar bar ($PA_{\rm mor} \approx 160^\circ$), extended radio jets (e.g. Cooke et al. 2000) and a Seyfert 2 nucleus (Baumgartner et al. 2013). A nuclear bar ($PA_{\rm mor} \approx 145^\circ$) has also been posited (e.g. Läsker et al. 2016). The presence of two compact X-ray sources separated by ≈130 pc suggests there are two SMBHs in the nuclear region (Fabbiano et al. 2011), but these may be due to noise (Koss et al. 2015), and subsequent radio, near-infrared, optical, UV, and hard X-ray observations are all consistent with a single point source (Imanishi & Saito 2014; Koss et al. 2015).

H_2O megamasers were discovered using the National Aeronautics and Space Administration (NASA) Deep Space Network (Kondratko et al. 2006), and mapped with very long baseline interferometry (VLBI) to infer a central SMBH mass $M_{\rm BH} = (3.0 \pm 0.2) \times 10^7\,{\rm M}_\odot$ at our adopted distance above (Kondratko et al. 2008). With the same data set, Huré et al. (2011) inferred a different SMBH mass of $M_{\rm BH} = 0.58 \times 10^7\,{\rm M}_\odot$ (at our adopted distance above) using different dynamical modelling. We therefore adopt the mean of these two measurements for the NGC 3393 SMBH mass, and half the difference as the uncertainty, as done by Kormendy & Ho (2013). The maser disc is large, with an outer radius of 1.5 pc, and was assumed to be edge-on with a tentative warp and $PA_{\rm kin} \approx 326^\circ$, perpendicular to both the kiloparsec-scale radio jet and the axis of the narrow-line region (see Kondratko et al. 2008 and references therein). The overall inclination of the galaxy is $i = 44^\circ$ with $PA_{\rm mor} \approx 160^\circ$, as determined from a Two Micron All Sky Survey (2MASS) $K_{\rm s}$-band image (Skrutskie et al. 2006).

CO (2–1) emission was recently mapped with ALMA by Finlez et al. (2018). They presented two sets of maps with different imaging parameters, one with a 0.″56 synthesized beam[4] and 2.5 km s^{-1} channels, the other with a 0.″68 synthesized beam and 10 km s^{-1} channels. Very little CO (2–1) emission is detected in the very centre, which they attribute to either molecular gas destruction by the jet or high molecular gas densities/temperatures not detected in the $J =$ 2–1 CO transition (see e.g. Mukherjee et al. 2018a, b; Ruffa et al. 2022). Our new observations slightly improve the angular resolution and sensitivity of these observations (see Table 3). Finlez et al. (2018) also provided a sophisticated analysis of the ionized-gas kinematics, exploiting abundant optical emission lines. In addition to a regularly rotating component, there are a jet-driven outflow along the jet axis and an equatorial outflow perpendicular to it. Reynolds et al. (2022) reported an extended H I disc with a diameter of 226 arcsec (54 kpc) and a total mass of $6.4 \times 10^9\,{\rm M}_\odot$ (scaled to our adopted distance above).

2.4 NGC 5765B

NGC 5765B is an Sab galaxy (Pjanka et al. 2017) with a Seyfert 2 nucleus (Toba et al. 2014). It has a close companion, NGC 5765A, at an angular separation of 22.″5 (≈12 kpc at our adopted distance below), beyond the FoV of our ALMA and JCMT observations. *HST* imaging reveals a bar, two rings (at radii of 1.″5 and 3.″5), and spiral features between these rings. Beyond the outer ring, the galaxy is perturbed by interaction with its companion (Pjanka et al. 2017).

Central megamasers were detected with the Green Bank Telescope as part of the MCP and were monitored for over two years, yielding an angular diameter distance $D = 112 \pm 5$ Mpc (adopted here; Pesce et al. 2020) and a SMBH mass $M_{\rm BH} = (4.0 \pm 0.4) \times 10^7\,{\rm M}_\odot$ (at this adopted distance; Gao et al. 2016). The maser disc (≈1.2 pc in radius) warps over an inclination range of $i = 94.^\circ5$ at the centre to $i =$ $73.^\circ3$ at the edge and over a kinetic position angle range of $PA_{\rm kin} =$ $146.^\circ7$ at the centre to $PA_{\rm kin} = 139.^\circ8$ at the edge, as determined through dynamical modelling (Gao et al. 2016). The overall galaxy inclination is $i = 26^\circ$ with $PA_{\rm mor} = 10^\circ$, as determined from a 2MASS $K_{\rm s}$-band image (Skrutskie et al. 2006).

Shirazi & Brinchmann (2012) studied the ionized gas of NGC5765B using an optical spectrum from SDSS. They reported strong nebular He II emission lines dominated by the AGN (i.e. without Wolf–Rayet features), along with other emission lines. The Arecibo Legacy Fast Arecibo *L*-band Feed Array survey (Haynes et al. 2018) derived a neutral hydrogen content of $(6.3 \pm 0.7) \times 10^9\,{\rm M}_\odot$ (at our adopted distance above). Davis et al. (2022) presented an ALMA CO (2–1) map and reported a total mass of $(1.2 \pm 0.1) \times 10^{10}\,{\rm M}_\odot$ (at our adopted distance above).

3 OBSERVATIONS

3.1 ALMA observations

Observations of the CO (2–1) line of our three target galaxies were carried out with ALMA as part of programme 2016.1.01553.S (PI: Bureau) on 2016 October 24, 2017 May 2, 2017 May 3, and 2017 May 15. For NGC 3393, we combine another track from ALMA programme 2015.1.00086.S (PI: Nagar) obtained on 2016 May 3.

For all our observations, the ALMA correlator was configured with one spectral window centred on the redshifted frequency of the CO (2–1) line (rest frequency $\nu_{\rm rest} = 230.538$ GHz.), with a bandwidth of 1.875 GHz (2438 km s^{-1} at $z = 0$) and 488-kHz channels (0.63 km s^{-1} at $z = 0$). The remaining three spectral windows were used to observe the continuum, if any, each with a bandwidth of 2 GHz and 15.625-MHz channels. The additional track for NGC 3393 also had one spectral window centred on CO (2–1), with an additional spectral-line window centred on CS (5–4) and two continuum spectral windows. Details of this track can be found in Finlez et al. (2018). The FoV of the ALMA 12-m array, i.e. the FWHM of the ALMA 12-m antenna primary beam, is ≈25 arcsec (≈7.0, 6.0, and 15 kpc for NGC 1194, NGC 3393, and NGC 5765B, respectively) at the observed frequencies of CO (2–1). This FoV only extends to 1.1 $R_{\rm e}$ in NGC 1194 (*H*-band combined with *K*-band; Läsker et al. 2016), 1.3 $R_{\rm e}$ in NGC 3393 (*H*-band combined with *I*-band; Läsker et al. 2016) and 1.8 $R_{\rm e}$ in NGC 5765B ($K_{\rm s}$-band; Davis et al. 2022), where $R_{\rm e}$ is the effective (i.e. half-light) radius. The ALMA FoV therefore covers the whole galaxy disc only in NGC 5765B, with more limited coverage in NGC 1194 and NGC 3393 (see Fig. 1)

The baseline ranges of the observations of NGC 1194, NGC 3393, and NGC 5765B were 19–1808, 15–1100, and 15–1124 m, respectively. The corresponding maximum recoverable scales were 2.″7 (0.86 kpc), 5.″1 (1.2 kpc), and 3.″5 (2.1 kpc), respectively. The data were calibrated using the standard ALMA pipeline, either through the European ALMA Regional Centre Calibrated Measurement Set (CalMS) service or by locally running `Common Astronomy Software Applications`[5] (`CASA`; CASA Team et al.

[4]Beam sizes quoted in this paper are all full-widths at half-maxima, FWHM.

[5]Available from https://casa.nrao.edu/.

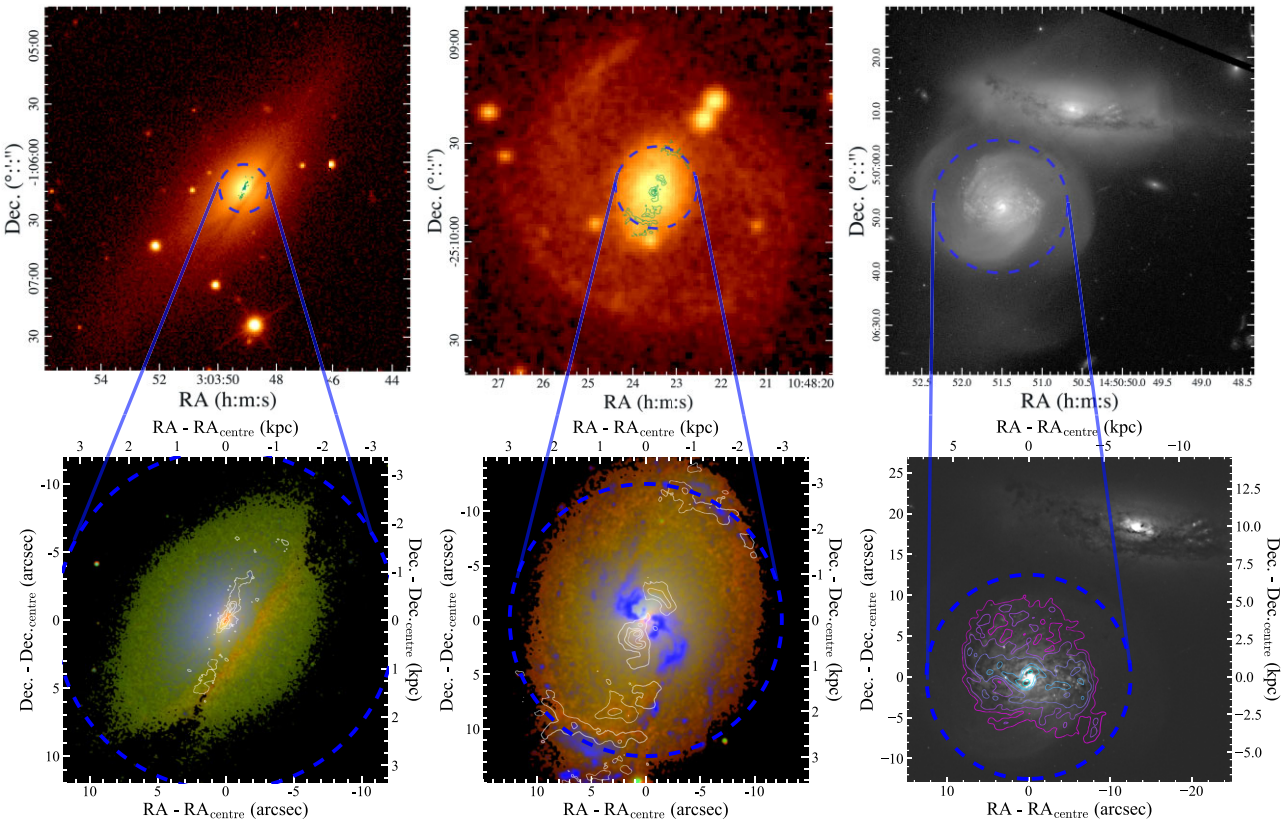

Figure 1. Optical images of our three target galaxies. In each panel, the ALMA CO (2–1) emission is overlaid as contours (except the upper-right-hand panel) and the ALMA primary beam is shown as a blue dashed circle. The bottom row panels show zoom-in images. *Left column:* NGC 1194. Upper panel: SDSS *r*-band image of the whole galaxy. Lower panel: *HST* Wide-field Camera 3 (WFC3) *F*438*W* (blue), *F*814*W* (green), and *F*160*W* (red) composite of the central region. *Middle column:* NGC 3393. Upper panel: Digitized Sky Survey-2 red-band image of the whole galaxy. Lower panel: *HST*/WFC3 *F*336*W* (blue), *F*814*W* (green), and *F*160*W* (red) composite of the central region. *Right column:* NGC 5765B (in the bottom-left corner of each panel) and its companion NGC 5765A. Upper panel: *HST*/WFC3 *F*814*W* image. Lower panel: unsharp-masked *HST*/WFC3 *F*814*W* image.

2022). CASA version 4.7 was used to calibrate the three tracks of 2016.1.01553.S and version 4.6 for the track of 2015.1.00086.S. For NGC 3393, the ALMA observations of Finlez et al. (2018) were combined with our higher-angular resolution observations to improve the *uv*-plane coverage and sensitivity (see Table 3). For both the line data cubes and the continuum images, the combined data improve the angular resolution (in one dimension) by ≈25 per cent compared to Finlez et al. (2018). The following imaging steps all used CASA version 6.4.4.

First, for each galaxy, continuum emission was subtracted from the visibility data using linear fits and the CASA task `uvcontsub`. To produce data cubes with high sensitivity, we binned the channels to 10 km s^{-1} and used Briggs weighting with a robust parameter of 2.0 (close to natural weighting). The data cubes were then cleaned to a depth of 1.5 times the root-mean-square (RMS) noise of the line-free channels using the task `tclean` with the `MultiScale` algorithm (Cornwell 2008) in the interactive mode and using a manually-defined three-dimensional mask. We note that varying these parameters does not significantly change any result of this paper. A primary beam correction was then applied to the line data cubes.

Moment maps were generated using a smooth-masking technique (e.g. Simon et al. 2024; Liang et al., in preparation). A smoothed data cube (without primary-beam correction) was first generated by spatially convolving every channel with a two-dimensional (2D) square uniform kernel of side length equal to the synthesized beam width. As the channels are already binned to a width of 10 km s^{-1}, we did not smooth further spectrally. We then constructed a mask by first selecting all pixels of the smoothed data cube above a given flux density threshold (1.5 RMS) and then excluding pixels outside of the mask manually defined during cleaning. Finally, the mask was adjusted channel by channel by (i) filling 'holes' of unselected pixels with areas smaller than two synthesized beams and (ii) removing 'islands' of selected pixels with areas smaller than one synthesized beam (both achieved using the Python package `scikit-image`;[6] van der Walt et al. 2014). This mask was then used to select the pixels of the original unsmoothed primary beam-corrected data cube that are used for the moment analysis.

The zeroth-moment (integrated flux), first-moment (intensity-weighted mean velocity), and second-moment[7] (intensity-weighted velocity dispersion) maps of NGC 1194, NGC 3393, and NGC 5765B are shown in the top rows of Figs 2, 3, and 4, respectively.

[6]Available from https://scikit-image.org.

[7]The second-moment requires at least two selected pixels along any line of sight, explaining the difference of spatial coverage between the second-moment map and other moment maps.

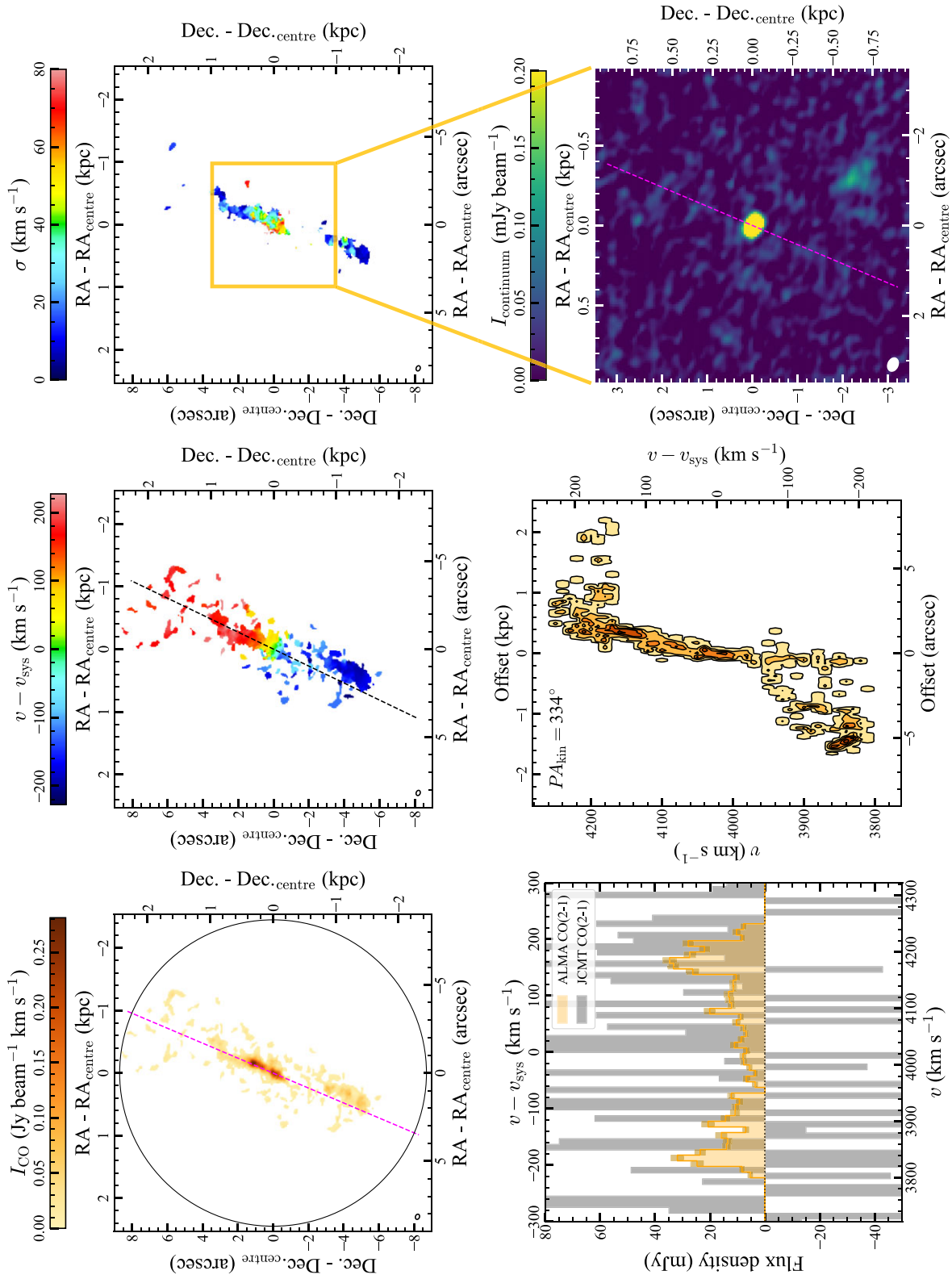

Figure 2. Data products of NGC 1194. *Top-left:* CO (2–1) zeroth-moment (integrated flux) map. The overlaid black solid circle shows the JCMT beam (assuming perfect pointing accuracy) at the same frequency. The magenta dashed line indicates the position angle of the maser disc (extrapolated in spatial extent). *Top-centre:* CO (2–1) first-moment (intensity-weighted mean velocity) map. The overlaid black dashed line shows the kinematic major axis. *Top-right:* CO (2–1) second-moment (intensity-weighted velocity dispersion) map. *Bottom-left:* CO (2–1) integrated spectrum synthesized from the ALMA data cube (orange histogram, with uncertainties indicated as darker shades) and JCMT spectrum (grey histogram). *Bottom-centre:* CO (2–1) PVD along the kinematic major axis, whose position angle is listed in the top-left corner. *Bottom-right:* 230-GHz continuum map. The magenta dashed line again indicates the position angle of the maser disc (extrapolated in spatial extent). The spatial extent shown is smaller than that of the moments maps, as illustrated by the overlaid orange square. The synthesized beam is shown in the bottom-left corner of all the maps.

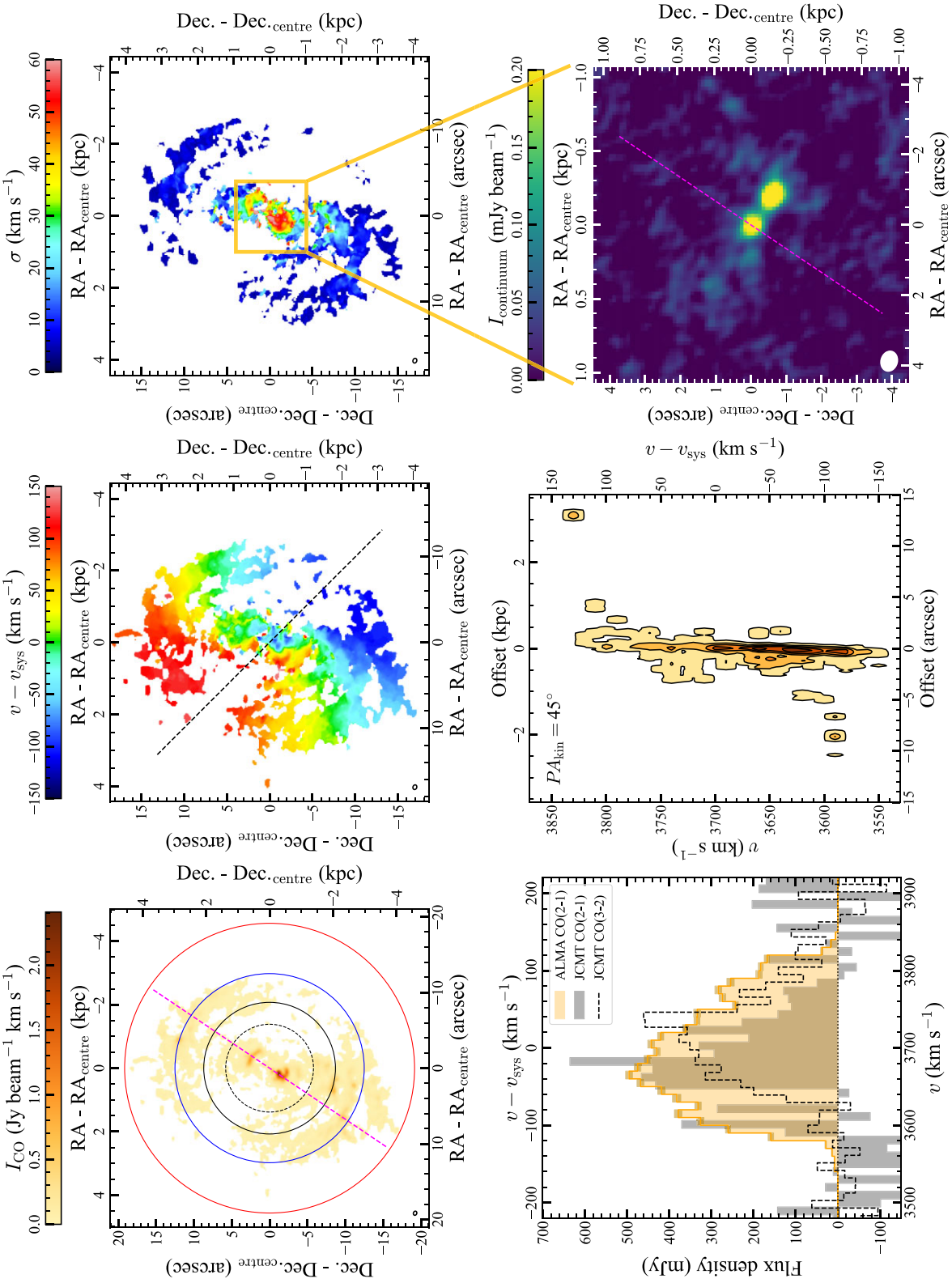

Figure 3. As Fig. 2 but for NGC 3393. The JCMT beam (assuming perfect pointing accuracy) at the CO (3–2) frequency is also shown in the top-left-hand panel as a black dashed circle, and the corresponding spectrum is shown in the bottom-left-hand panel as a black dashed histogram. The ALMA CO (2–1) primary beam full width at 50 per cent (i.e. the usual primary beam definition) and at 20 per cent (the maximal extent of the data cube) of the maximum are also shown in the top-left-hand panel as blue and red solid circles, respectively. Due to the scarcity of gas along the kinematic major axis, the kinematic position angle of 45° was estimated by eye rather than by a fit. The CO (2–1) emission reaches the edge of the ALMA FoV.

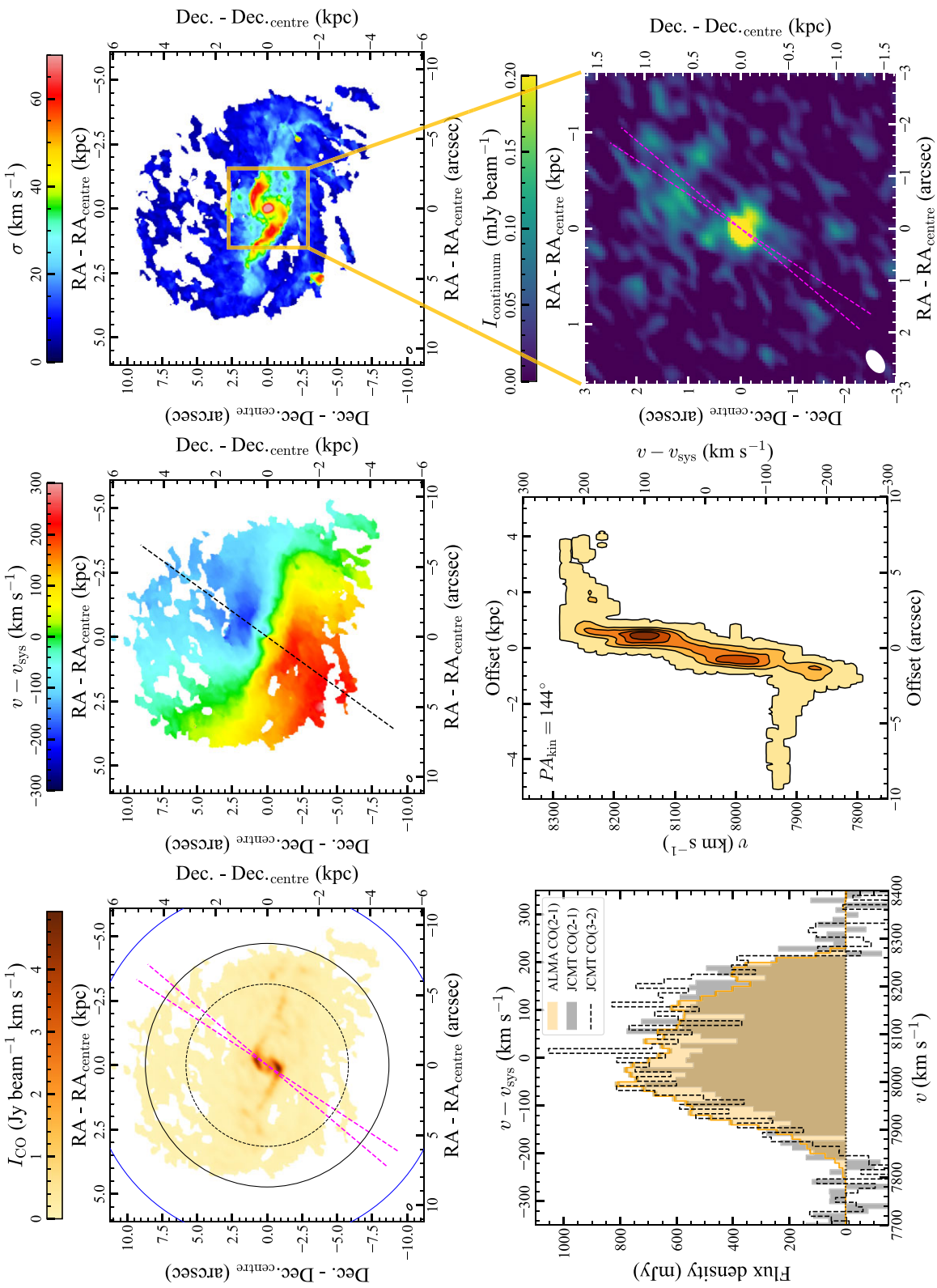

Figure 4. As Fig. 3 but for NGC 5765B (although the red solid circle is not visible and the range of position angles of the maser disc due to its warp is indicated by two magenta dashed lines in the relevant panels).

The same mask was used to create the integrated spectrum (and to calculate the integrated flux) and the kinematic majoraxis position-velocity diagram (PVD) of each galaxy, shown in the bottom-left and bottom-centre panel of each figure, respectively. As each channel has a different 2D masked region and spaxels near each other are strongly correlated, we applied the following procedure to estimate the uncertainty of the spatially integrated flux of each channel. For each line channel, we applied its 2D mask to every line-free channel of the data cube, calculated the sum of the flux densities of each of those line-free channels and adopted the RMS (around the mean) of these sums as the uncertainty of the integrated flux of the original line channel. Standard error propagation rules[8] were then used to calculate the uncertainty of the flux integrated over all channels (and in turn of the total molecular gas mass). Each PVD was generated by adopting a 2 arcsec-wide mock slit along the kinematic major axis, determined from a fit to the first-moment map using the `pafit` software[9] (Krajnović et al. 2006), except for NGC 3393 for which a rough kinematic major axis position angle was estimated by visual inspection due to the scarcity of gas along it. We used the astrometry from the existing VLBI observations to define the centre of each galaxy (see Table 2).

For each galaxy, a continuum image was also produced from all spectral windows using only line-free channels. With the `tclean` task in the multifrequency synthesis mode, we again adopted Briggs weighting with a robust parameter of 2.0 and cleaned to a depth of 1.5 times the RMS noise of the dirty image (measured in emission-free regions) in the interactive mode and using a manually-defined 2D mask. The primary beam correction was then applied to the continuum images.

The final angular resolution, sensitivity, and other characteristics of each data product are listed in Table 3.

3.2 JCMT observations

Single-dish CO (2–1) observations of NGC 1194, NGC 3393, and NGC5765B were obtained with the JCMT on 2016 October 18–23, as part of Programme M16BP068 (PI: Gao), aiming to estimate the prevalence and abundance of molecular gas in the 15 disc galaxies known to harbour megamasers at the time and another 15 galaxies used as a control sample (Gao et al., in preparation). Follow-up CO (3–2) observations of NGC 3393 and NGC 5765B were carried out on 2017 July 6, 2017 December 5, 2018 January 22, 2018 January 29, and 2018 December 24, as part of Programme M17BP056 (PI: Gao).

The JCMT has a 15-m diameter antenna and therefore beams (i.e. FoVs) of 17.″4 and 11.″6 at the rest frequency of CO (2–1) and of CO (3–2), respectively, both of which are smaller than the ALMA primary beam in this work. Table 4 lists the basic properties of the JCMT observations, while the CO (2–1) and CO (3–2) JCMT beams are shown in Figs 2–4 as black solid and black dashed circles, respectively, overlaid on the zeroth-moment maps.

For the CO (2–1) observations, the RxA receiver was used with dual sidebands, with the Auto Correlation Spectral Imaging System (ACSIS) correlator configured to have a bandwidth of 1 GHz and channels of 1 MHz (≈1.3 km s^{-1} at $z = 0$). The observations were conducted in standard position-switching mode with a total on-source integration time of ≈30 min per target. For the CO (3–2) observations, the 16-pixel Heterodyne Array Receiver Program (HARP) was used, with the ACSIS correlator configured to have a bandwidth of 1 GHz and channels of 0.488 MHz (≈0.4 km s^{-1} at $z = 0$). The observations were conducted in beam-switching mode to achieve a better spectral baseline, with a total on-source integration time of ≈1 h per target.

For both CO (2–1) and CO (3–2) data reduction, the standard ORAC data reduction pipeline (ORAC-DR; Jenness & Economou 2015) was used within the `Starlink` software package[10] (Currie et al. 2014). The spectra were first rebinned to channels of 10 km s^{-1} to match our ALMA data. A linear baseline fit to line-free channels was then subtracted from each spectrum, to remove any continuum emission and non-flat baseline. The spectra were then converted to a flux density scale $S_\nu = 15.6\, T_A^\star/\eta_A$, where $T_A^\star$ is the antenna temperature and $\eta_A = 0.52$ is the JCMT antenna efficiency at both frequencies. The resulting spectra of NGC 1194, NGC 3393, and NGC 5765B are shown in the bottom-left-hand panels of Figs 2, 3, and 4, respectively.

The integrated flux of each spectrum was obtained by integrating over the velocity range with clear emission (or a range estimated from the ALMA data in the case of NGC 1194, which is a non-detection), as listed in Table 4, while the integrated flux uncertainty is estimated using

$$\sigma = \Delta v\, \sigma_{\rm chan} \sqrt{N_{\rm line}\left(1 + \frac{N_{\rm line}}{N_{\rm noise}}\right)}, \quad (1)$$

where Δv is the channel width (10 km s^{-1}), $\sigma_{\rm chan}$ the noise per channel listed in Table 4, $N_{\rm line}$ the number of channels used for the integration, and $N_{\rm noise}$ the number of channels used to estimate the noise (see Young et al. 2011). As for the ALMA data, the molecular gas mass of each galaxy was then calculated from the CO (2–1) line by assuming a CO (2–1)/CO (1–0) line ratio R_{21} of unity (in brightness temperature units) and a CO-to-molecule conversion factor $\alpha_{\rm CO} = 4.3\,{\rm M}_\odot\,{\rm pc}^{-2}\,({\rm K\,km\,s}^{-1})^{-1}$ (Bolatto, Wolfire & Leroy 2013), including the contribution of heavy elements, yielding

$$\frac{M_{\rm mol}}{{\rm M}_\odot} = \frac{2.63\times10^3}{1+z_{\rm helio}} \left(\frac{F_{\rm CO(2\text{-}1)}}{\rm Jy\,km\,s^{-1}}\right)\left(\frac{D}{\rm Mpc}\right)^2, \quad (2)$$

where $F_{\rm CO\,(2-1)}$ is the intregrated CO (2–1) flux density.

3.3 NGC 1194

3.3.1 *Molecular gas*

The moment maps, PVD, and integrated spectrum of NGC 1194 shown in Fig. 2 suggest an edge-on, disturbed and lopsided central molecular gas disc well aligned with the maser disc. There are two large molecular gas concentrations, one extending north-west from the centre, the other farther out and disconnected to the south-east. Comparison to the SDSS *r*-band image in the upper-left-hand panel of Fig. 1 reveals the concentrations to be roughly aligned with the galaxy morphological major axis, while the composite *HST* image (*F*438*W*, *F*814*W,* and *F*160*W* filters) in the lower-left-hand panel of Fig. 1 shows the molecular gas to be associated primarily with a weak irregular dust lane crossing the galaxy centre (with $PA_{\rm mor} \approx 160^\circ$), while a much more prominent dust lane (offset to the south-west with $PA_{\rm mor} \approx 145^\circ$) that seems to define part of a dust ring is apparently devoid of CO emission. This morphology and the first-moment map suggest the molecular gas to be part of an irregular

[8]Given the raw spectral resolution and the binned channel width, we safely assume no covariance between adjacent channels.
[9]Available from https://pypi.org/project/pafit/.
[10]Available from https://starlink.eao.hawaii.edu/starlink .

Table 2. Properties of our target galaxies.

Galaxy	Right ascension (J2000)	Declination (J2000)	$z^{1}_{\rm helio}$	Hubble type	Nuclear activity
NGC 1194	$03^{\rm h}03^{\rm m}49\overset{\rm s}{.}10870^{2}$	$-01^{\circ}06'13\overset{''}{.}4720^{2}$	0.01363	S0-[3]	Sy2[4]
NGC 3393	$10^{\rm h}48^{\rm m}23\overset{\rm s}{.}4659^{5}$	$-25^{\circ}09'43\overset{''}{.}477^{5}$	0.01251	SBa[6]	Sy2[4, 7]
NGC 5765B	$14^{\rm h}50^{\rm m}51\overset{\rm s}{.}51884^{8}$	$+05^{\circ}06'52\overset{''}{.}2501^{8}$	0.02754	Sab[9]	Sy2[10]

Notes. (1) Heliocentric redshifts are taken from Albareti et al. (2017) for NGC 1194 and NGC 5765B and from Pesce et al. (2015) for NGC 3393. (2) Average position of the masers at the systemic velocity of the galaxy (see Tables 1 and 3 of Kuo et al. 2011). (3) Nair & Abraham (2010). (4) Oh et al. (2018). (5) Average position of the masers at the systemic velocity of the galaxy (see Section 4 of Kondratko et al. 2008). (6) de Vaucouleurs et al. (1991). (7) Baumgartner et al. (2013). (8) Best-fitting dynamical centre (see Table 7 of Gao et al. 2016). (9) Pjanka et al. (2017). (10) Toba et al. (2014).

structure embedded within a roughly edge-on rotating disc, itself aligned with the large-scale galaxy disc. Unsurprisingly, the second-moment map reveals irregular velocity dispersions. The velocity dispersions are highest in the centre, but this may be due to beam smearing. They decrease to 10–20 km s^{-1} at the extremities of the distribution, typically associated with dynamically cold gas, and are comparable to the velocity dispersions of discs reported in other works (e.g. Davis et al. 2018; Smith et al. 2019; Lelli et al. 2022; Lu et al. 2022). Overall, our observations suggest a disturbed molecular gas distribution in a non-equilibrium state, possibly caused by an earlier (minor) merger event, an hypothesis supported by the twisted morphological position angle at large radii (see fig. 11 of Läsker et al. 2016) as well as the existence of a detached H I cloud to the north-west of the main galaxy disc (Sun et al. 2013). Despite this, the maximum rotation velocity matches well that measured in H I (Sun et al. 2013).

As shown in the bottom-left-hand panel of Fig. 2, NGC 1194 is not detected in our JCMT CO (2–1) observations, that have a sensitivity of only 83 mJy per channel (while our synthesized ALMA integrated spectrum has a sensitivity of 1.3 mJy per channel on average, both based on the same channel width of 10 km s^{-1}). The ALMA integrated flux of 6.1 $\pm$ 0.1 Jy km s^{-1} yields a total molecular gas mass of (5.3 $\pm$ 0.1) $\times$ 10^{7} M$_{\odot}$. Here and for the other two galaxies, the uncertainties quoted on the integrated flux and associated integrated mass are exclusively due to the noise in the integrated spectrum (see Section 3.1). They do not include potential systematic errors such as the ALMA flux calibration uncertainty (typically ≈10 per cent), CO-to-molecule conversion factor uncertainty (typically ≈30 per cent; Bolatto et al. 2013), galaxy distance uncertainty (typically ≈10 per cent), etc. As the ALMA and JCMT FoVs only encompass ≈1 $R_{\rm e}$ around the galaxy centre, we have no information on the molecular gas beyond that region, and both the integrated flux and the associated integrated mass calculated here are likely lower limits of those quantities for the entire galaxy.

3.3.2 230-GHz continuum emission

The continuum map shown in the bottom-right-hand panel of Fig. 2 reveals a single compact 230-GHz continuum source at the centre of NGC 1194, most likely associated with the AGN. Fitting this source with a 2D Gaussian, using the `CASA` task `imfit` reveals it to be slightly spatially resolved (i.e. slightly larger than the synthesized beam). Its position and flux density derived from the Gaussian fit are listed in Table 5. This position is marginally consistent with that derived from maser astrometry (see Table 2). Another tentative more diffuse source is located ≈2$\overset{''}{.}$4 south-west of the centre, with an integrated flux of ≈0.55 mJy.

3.4 NGC 3393

3.4.1 Molecular gas

The moments maps, PVD, and integrated spectra of NGC 3393 shown in Fig. 3 suggest a fairly regular but patchy molecular gas distribution, with little gas near the kinematic major axis and only faint diffuse gas in the very centre. There are two brighter structures in the central region, one south-east of the centre (≈1$\overset{''}{.}$5 or 360 pc from the centre), the other to the north-west (≈3$\overset{''}{.}$3 or 790 pc from the centre), whose morphologies are reminiscent of (part of) a nuclear ring and/or spiral. These are also associated with increased velocity dispersions (40–60 km s^{-1}) that are otherwise ordinary (10–20 km s^{-1}). The velocity field is fairly regular on large scales, with $PA_{\rm kin}$ ≈ 45°, although a kinematic twist is present in the outer parts (most easily seen as a clear kink in the zero-velocity curve) and there are many small-scale disturbances. Finlez et al. (2018) discussed the observed CO (2–1) kinematics in great detail, along with the stellar and ionized-gas kinematics. To explain both the large-scale kinematics and that near the two brighter sources, they proposed a perturbation model driven by both a large-scale bar and a nuclear bar. The molecular gas detected at the largest radii (≈10 arcsec) forms an annulus or ring-like structure, that may be associated with spiral arms observed in the UV (see the lower-middle panel of Fig. 1), and may thus trace recent star formation. Finally, the lack of molecular gas along the kinematic major axis may be due to photo-ionization by the AGN/jets detected in continuum emission (see below), that are perpendicular to the accretion disc traced by maser emission (magenta lines in Fig. 3).

As shown in the bottom-left-hand panel of Fig. 3, our JCMT CO (2–1) spectrum is in good agreement with our synthesized ALMA integrated spectrum at velocities above 3650 km s^{-1}, but the two differ at smaller velocities, with much lower JCMT fluxes. The ALMA first-moment map indicates that this could be accounted for if the JCMT had a pointing offset. Independent of this, despite the fact that our ALMA data do not have baselines shorter than 15 m, ALMA generally recovers more flux than the JCMT, likely because of the smaller FoV of the latter and the extended molecular gas distribution. The integrated flux of our ALMA CO (2–1) cube is 81.8 $\pm$ 0.4 Jy km s^{-1}, yielding a total molecular gas mass of (5.14 $\pm$ 0.02) $\times$ 10^{8} M$_{\odot}$. As the ALMA FoV only encompasses ≈1.3 $R_{\rm e}$ and the molecular gas clearly extends to the FoV's edge, both the integrated flux and the associated integrated mass should again be considered lower limits of those quantities for the entire galaxy.

Our CO (3–2) JCMT spectrum is also in good agreement with our synthesized ALMA integrated CO (2–1) spectrum at velocities above 3720 km s^{-1}, but it again shows a significant flux deficit at

Table 3. Properties of our ALMA CO (2–1) and 230-GHz continuum observations. NGC 3393 includes the properties of Finlez et al.'s (2018) observations for reference.

Galaxy	Property	Value
NGC 1194:	Baseline range (m)	19–1808
	Maximum recoverable scale (arcsec)	2.7
	On-source time (min.)	19.75
	Pixel scale (arcsec pix^{-1})	0.05
	CO channel width (km s^{-1})	10
	CO synthesized beam (arcsec)	0.30 × 0.23
	CO synthesized beam (pc)	84 × 65
	CO RMS noise (mJy beam^{-1} chan^{-1})	0.41
	CO integrated flux[1] (Jy km s^{-1})	6.1 ± 0.1
	Integrated molecular gas mass[2] (M$_\odot$)	(5.3 ± 0.1) × 10^7
	Cont. rest-frame frequency (GHz)	232.1
	Cont. synthesized beam (arcsec)	0.31 × 0.22
	Cont. synthesized beam (pc)	87 × 62
	Cont. RMS noise (mJy beam^{-1})	0.020
NGC 3393:[3]	Baseline range (m)	15–1100
	Maximum recoverable scale (arcsec)	5.1
	On-source time of (min.)	49.07
	Pixel scale (arcsec pix^{-1})	0.1
	CO channel width (km s^{-1})	10
	CO synthesized beam (arcsec)	0.56 × 0.45
	CO synthesized beam (pc)	136 × 107
	CO RMS noise (mJy beam^{-1} chan^{-1})	0.37
	CO integrated flux[1] (Jy km s^{-1})	81.8 ± 0.4
	Integrated molecular gas mass[2] (M$_\odot$)	(5.14 ± 0.02) × 10^8
	Cont. rest-frame frequency (GHz)	238.7
	Cont. synthesized beam (arcsec)	0.58 × 0.47
	Cont. synthesized beam (pc)	138 × 112
	Cont. RMS noise (mJy beam^{-1})	0.017
NGC 3393:[4]	Baseline range (m)	15–629
	Maximum recoverable scale (arcsec)	5.3
	On-source time (min.)	28.33
	CO channel width (km s^{-1})	10
	CO synthesized beam (arcsec)	0.73 × 0.62
	CO synthesized beam (pc)	174 × 148
	CO RMS noise (mJy beam^{-1} chan^{-1})	0.45
	Cont. rest-frame frequency (GHz)	239.6
	Cont. synthesized beam (arcsec)	0.71 × 0.61
	Cont. synthesized beam (pc)	169 × 146
	Cont. RMS noise (mJy beam^{-1})	0.023
NGC 5765B:	Baseline range (m)	15–1124
	Maximum recoverable scale (arcsec)	3.5
	On-source time (min.)	22.25
	Pixel scale (arcsec pix^{-1})	0.06
	CO channel width (km s^{-1})	10
	CO synthesized beam (arcsec)	0.47 × 0.28
	CO synthesized beam (pc)	257 × 153
	CO RMS noise (mJy beam^{-1} chan^{-1})	0.48
	CO integrated flux[1] (Jy km s^{-1})	216.2 ± 0.4
	Integrated molecular gas mass[2] (M$_\odot$)	(6.94 ± 0.01) × 10^9
	Cont. rest-frame frequency (GHz)	232.5
	Cont. synthesized beam (arcsec)	0.47 × 0.28
	Cont. synthesized beam (pc)	257 × 153
	Cont. RMS noise (mJy beam^{-1})	0.028

Notes. [1] The CO integrated fluxes and associated integrated molecular gas masses are measured within the ALMA FoV only, and thus likely do not cover the full molecular gas extent of NGC 1194 and NGC 3393.

[2] A CO (2–1)/CO (1–0) line ratio of unity (in brightness temperature units) and a CO-to-molecule conversion factor of 4.3 M$_\odot$ pc^{-2} (K km s^{-1})$^{-1}$ are assumed to infer the molecular gas masses, that include the contribution of heavy elements.

[3] All the quantities listed in this segment are measured after combining the observations from programmes 2016.1.01553.S and 2015.1.00086.S.

[4] All the quantities listed in this segment are taken from Finlez et al. (2018).

Table 4. Properties of our JCMT CO (2–1) and CO (3–2) observations.

Galaxy	Property	Value
NGC 1194	Velocity range (km s^{-1})	3800–4300
	CO (2–1) RMS noise (mJy)	83
	CO (2–1) int. flux (Jy km s^{-1})	<17.8
	$M_{\rm mol}$ (M$_\odot$)	<1.55 × 10^8
NGC 3393	Velocity range (km s^{-1})	3580–3900
	CO (2–1) RMS noise (mJy)	131
	CO (2–1) int. flux (Jy km s^{-1})	43 ± 10
	$M_{\rm mol}$ (M$_\odot$)	(2.7 ± 0.6) × 10^8
	CO (3–2) RMS noise (mJy)	71
	CO (3–2) int. flux (Jy km s^{-1})	52 ± 5
	JCMT CO (2–1)/CO (3–2) (K/K)	1.8 ± 0.5
NGC 5765B	Velocity range (km s^{-1})	7750–8400
	CO (2–1) RMS noise (mJy)	115
	CO (2–1) int. flux (Jy km s^{-1})	186 ± 16
	$M_{\rm mol}$ (M$_\odot$)	(6.0 ± 0.5) × 10^9
	CO (3–2) RMS noise (mJy)	67
	CO (3–2) int. flux (Jy km s^{-1})	207 ± 14
	JCMT CO (2–1)/CO (3–2) (K/K)	2.02 ± 0.22

Note. The integrated CO fluxes and associated integrated molecular gas masses and CO line ratios are only measured within the JCMT FoVs, that do not necessarily cover the full extent of the galaxies' molecular gas. The RMS noises were measured using a channel width of 10 km s^{-1}.

Table 5. Properties of compact 230-GHz sources within the fields of view of our observations.

Galaxy	Property	Value
NGC 1194	R.A. (J2000)	03^{h}03^{m}49^s.109
	Dec. (J2000)	−1°06′13″.48
	Flux (mJy)	1.73 ± 0.04
NGC 3393 (nucleus)	R.A. (J2000)	10^{h}48^{m}23^s.47
	Dec. (J2000)	−25°09′43″.5
	Flux (mJy)	0.40 ± 0.04
	Spectral index	−0.18 ± 0.03
NGC 3393 (SW)	R.A. (J2000)	10^{h}48^{m}23^s.40
	Dec. (J2000)	−25°09′44″.1
	Flux (mJy)	0.60 ± 0.04
	Spectral index	−0.8 ± 0.3
NGC 5765B (nucleus)	R.A. (J2000)	14^{h}50^{m}51^s.52
	Dec. (J2000)	+5°06′52″.2
	Flux (mJy)	0.71 ± 0.08
NGC 5765B (SW)	RA (J2000)	14^{h}50^{m}51^s.50
	Dec. (J2000)	+5°06′51″.9
	Flux (mJy)	0.28 ± 0.08

Notes. Source positions and integrated fluxes were measured using Gaussian fits. The spectral indices of NGC 3393 were measured by cross-identifying the sources with Very Large Array observations by Koss et al. (2015) and fitting power laws of the form $S \propto \nu^\alpha$ to the spectral energy distributions, where S is the integrated flux density, ν the frequency and α the spectral index.

lower velocities. This could again be explained by a pointing offset. The integrated JCMT CO (3–2) flux of 52 ± 5 Jy km s^{-1} is thus both highly unreliable and likely a lower limit.

3.4.2 230-GHz continuum emission

The 230-GHz continuum map shown in the bottom-right-hand panel of Fig. 3 reveals two compact sources, one at the galaxy centre, consistent with the VLBI maser location, that we will refer to as the

nuclear source, the other offset by ≈1.″0 or ≈240 pc south-west of the nucleus. Both sources are marginally spatially resolved, and the south-west source is ≈50 per cent brighter than the nuclear source. There is also faint fuzzy emission north-east of the nucleus.

Based on X-ray emission, Fabbiano et al. (2011) reported a pair of SMBH/AGN separated by 150 pc (0.″6), much smaller than the separation of ≈240 pc between the two 230-GHz compact sources discussed above. Comparing the positions of the two X-ray sources in fig. 1 of Fabbiano et al. (2011), they appear to both be located in the emission tail of our nuclear source, both far away from the south-west compact source. Therefore, our two compact sources are unlikely to be Fabbiano et al.'s (2011) claimed dual SMBH/AGN. We also note that while Finlez et al. (2018) also disfavoured a SMBH/AGN pair, they misreported the location of the claimed second source in their fig. 4 and section 4.3 which, according to fig. 1a of Fabbiano et al. (2011), should be north-east of the peak of the Very Large Array's (VLA) 8.4-GHz central source.

The nuclear source overlaps with component A discovered by Koss et al. (2015; also reported by Finlez et al. 2018) using VLA 8.4- and 4.9-GHz continuum observations, while the south-west compact source partially overlaps with their component B. A third source north-east of the centre was also reported by both Koss et al. (2015) as their component C and by Finlez et al. (2018). By carefully checking the spatial extent of component C, we conclude that the fuzzy emission detected here north-east of the nucleus also overlaps with it.

These three sources (nuclear source, south-west compact source, and north-east fuzzy emission) can be attributed to the central AGN and (intrinsically) symmetric jets on both sides of it. The south-west compact source is associated with the approaching jet and is thus significantly brighter than the north-east fuzzy emission (associated with the receding jet) due to Doppler-boosting (Koss et al. 2015). The integrated fluxes of the two compact sources are reported in Table 5, again derived using 2D Gaussian fits carried out with the `CASA` task `imfit`. Combining our measurements with those of Koss et al. (2015) at 8.4 and 4.9 GHz, we fit power laws of the form $S \propto \nu^{\alpha}$ to the spectral energy distributions, where S is the integrated flux density, ν the frequency and α the spectral index, and estimate that the nuclear source has a spectral index $\alpha = -0.18 \pm 0.03$ while the south-west compact source (i.e. the approaching jet) has $\alpha = -0.8 \pm 0.3$ (see Fig. 5). These spectral indices are within the range of spectral indices of other nuclei and jets (e.g. Hovatta et al. 2014), and are consistent with self-absorbed optically thick synchrotron emission in the nucleus and optically thin synchrotron emission in the jet (see e.g. Ruffa et al. 2019a, 2022). We note, however, that we have neither matched our resolution to that of the VLA observations nor applied a 15σ cut as done by Koss et al. (2015). These could lead to a bias in the spectral indices estimated.

3.5 NGC 5765B

3.5.1 Molecular gas

The CO (2–1) emission of NGC 5765B is very strong. The moment maps shown in Fig. 4 show the typical morphology and dynamics of a barred disc galaxy, with emission particularly strong along two bisymmetric dust lanes (parallel to but offset from the optical bar; see the right column of Fig. 1) as well as two bisymmetric nuclear spiral arms. The velocity field in turn shows a very strong kinematic twist beyond the dust lanes and thus the bar (most easily seen as a clear kink in the zero-velocity curve), and a milder kinematic twist in the centre within the nuclear spiral. We note that the sudden velocity

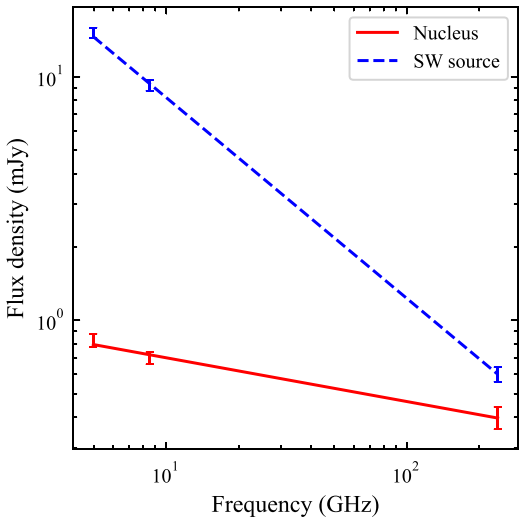

Figure 5. Radio – millimetre integrated continuum flux densities and power-law fits of the nuclear source (red) and south-west compact source (blue) detected in NGC 3393. The 8.4- and 4.9-GHz measurements are from Koss et al. (2015).

jumps detected in the PVD within ≈2 arcsec on either side of the galaxy centre are not the signatures of Keplerian rotation around a putative SMBH, but rather arise from the bar and the twisted velocity map. As expected, the velocity dispersion map shows broad line-widths ($\sigma \gtrsim 40\,\mathrm{km\,s^{-1}}$) due to beam smearing along the offset dust lanes, which are probably tracing bisymmetric shocks along the leading edges of the bar (see e.g. Athanassoula 1992; Athanassoula & Beaton 2006; Kim & Stone 2012), and in the very centre, that may also harbour gas with intrinsically high turbulence due to AGN and/or star-formation feedback. There are also mildly increased line-widths slightly beyond the end of the dust lanes (slightly leading). The gas elsewhere is dynamically cold ($\sigma < 20\,\mathrm{km\,s^{-1}}$) and follows a regular rotation pattern. We do nevertheless note a slight excess of molecular gas in the northern half of the galaxy, which may be related to the gravitational interaction with NGC 5765B's companion galaxy NGC 5765A. Another galaxy with a very similar barred morphology has recently been studied at much higher spatial resolution (24 pc) as part of the WISDOM project (NGC 5806; Choi et al. 2023).

As shown in the bottom-left panel of Fig. 4, our JCMT CO (2–1) spectrum (integrated flux density $186 \pm 16\,\mathrm{Jy\,km\,s^{-1}}$, corresponding to an integrated molecular gas mass of $(6.0 \pm 0.5) \times 10^9\,\mathrm{M_\odot}$) is in good agreement with our synthesized ALMA integrated spectrum ($216.2 \pm 0.4\,\mathrm{Jy\,km\,s^{-1}}$ and $(6.94 \pm 0.01) \times 10^9\,\mathrm{M_\odot}$). The slight difference is likely due to the primary beam of the JCMT being slightly smaller than the total extent of the molecular gas detected with ALMA. Due to the relatively large distance of this galaxy, the ALMA primary beam reaches ≈1.8 R_e, well beyond the total extent of the molecular gas detected, so all the molecular gas of NGC 5765B has probably been detected. The JCMT CO (3–2) spectrum is very similar to the CO (2–1) spectrum, the small differences probably reflecting minor excitation and/or distribution differences.

3.5.2 230-GHz continuum emission

The 230-GHz continuum map shown in the bottom-right-hand panel of Fig. 4 reveals one bright nuclear compact source (taking the VLBI source as the galaxy centre), a fainter compact source ≈0.″4 (≈200 pc) to the south-west of the centre and fuzzy extended emission to the

north-west of the centre. Considering their locations, compactness, and relative orientation (perpendicular to the maser disc), the two compact sources are likely due to the AGN (the off-centre source perhaps tracing a young jet). The fuzzy emission to the north-west partially overlaps with high surface brightness and/or high velocity dispersion regions in the zeroth- and second-moment maps. It may be dust emission, but nothing is detected on the opposite side of the galaxy despite a bisymmetric molecular gas distribution. Multiband radio observations should constrain the spectral indices and therefore help reveal the origin of these sources.

4 POTENTIAL FOR SMBH MASS MEASUREMENTS

Based on the detailed descriptions of the previous section, we now discuss the potential of each galaxy for a SMBH mass measurement using CO kinematics and future higher angular resolution ALMA observations ($\sim$0.″01).

NGC 1194 has a narrow, lopsided, and disturbed molecular gas distribution (see Section 3.3) that would prevent any robust dynamical modelling. In any case, it has very little molecular gas (see Fig. 2), and the faintness of the CO (2–1) emission would result in impractically long exposure times with any synthesized beam much smaller than the current one. For a quantitative estimate, we take the brightest pixel across the central synthesized beam and all channels of the current data cube (with a flux of 2.95 mJy beam^{-1} at 4030 km s^{-1}), assume a homogeneous molecular gas distribution within it and adopt a smaller synthesized beam of 0.″045 required to marginally spatially resolve the predicted angular radius of the SMBH SoI ($\theta_{\rm SoI} = 0.''050$; see Table 1). Requiring a signal-to-noise ratio $S/N = 5$ per synthesized beam and 10 km s^{-1} channels, we estimate using the ALMA Observing Tool (OT) that the observations would require a total observing time of $\approx$70 days.

Another uncertainty of course is that while the gas kinematics is consistent with a regular rotating disc at the current angular resolution, it is possible that at higher angular resolutions the very centre (at the scale of the SMBH SoI) would be disturbed or have a much lower CO surface brightness (e.g. a central hole), as is the case in several galaxies (e.g. Davis et al. 2018; Smith et al. 2019; Ruffa et al. 2023). This concern of course applies to all galaxies, those discussed here and others.

NGC 3393 has a fairly regular molecular gas distribution and kinematics at large spatial scales (see Section 3.4), but there are many substructures and kinematic disturbances at small scales, and Finlez et al. (2018) required both a large-scale bar and a nuclear bar to model the kinematics. Such kinematic complexity would make it extremely difficult to robustly infer a SMBH mass through dynamical modelling. This difficulty would be compounded by the faintness of the CO (2–1) emission in the very centre and the lack of gas along the kinematic major axis (see Fig. 3), the regions that best constrain the SMBH mass. In any case, for a central peak intensity of 2.38 mJy beam^{-1} at 3630 km s^{-1}, and requiring the smallest synthesized beam currently provided by ALMA (0.″02) to attempt to spatially resolve the predicted $R_{\rm SoI}$ ($\theta_{\rm SoI} = 0.''013$; see Table 1), estimating the required ALMA observation time as above results in a total of $\approx$100 years.

The molecular gas distribution and kinematics of NGC 5765B are typical of those of barred disc galaxies (see Section 3.5). While this would make it challenging to model the large-scale kinematics, with sufficient spatial resolution it may be possible to model what appears to be a decoupled central disc (within the nuclear spiral and inner kinematic twist). The high velocity dispersions in the very centre are consistent with such a fast rotating disc. However, while having relatively bright CO (2–1) emission, with a peak central intensity of 27.4 mJy beam^{-1} at 8190 km s^{-1}, the small angular scale required to resolve the predicted $R_{\rm SoI}$ ($\theta_{\rm SoI} = 0.''013$; see Table 1) leads to an impossible integration time. Indeed, requiring a synthesized beam of 0.″02 (the smallest currently available) and estimating the required ALMA observation time as above results in a total of $\approx$80 days.

Overall, because primarily of the impossibly long observation times required, and to a lesser extent the disturbed gas kinematics, none of our three target is ultimately suitable for a SMBH mass measurement using ALMA. Of course, we have assumed here that CO is the most abundant cold molecular gas tracer in these three galaxies, and that observing CO (2–1) yields the best balance between S/N and angular resolution, but we cannot rule out the possibility that another cold molecular gas tracer (e.g. higher CO transition or higher-density tracer) might be better suited to measure the SMBH masses in these galaxies.

Apart from the intrinsic faintness of CO (2–1) in NGC 1194 and NGC 3393, the long observation times are primarily driven by the extremely small $\theta_{\rm SoI}$ required, as the observation time-scales with the negative fourth power of $\theta_{\rm SoI}$ at a given surface brightness. In turn, the small $\theta_{\rm SoI}$ have primarily two causes. First, the maser method mostly probes low-mass SMBHs ($M_{\rm BH} \sim 10^7$ M$_\odot$, lower than most successful SMBH mass measurements using cold molecular gas), yielding small $R_{\rm SoI}$. Second, because of the scarcity of masers, maser-hosting galaxies are on average rather distant, much farther than most galaxies with existing SMBH mass measurements (the few nearby potential targets considered in Section 2.1 did not satisfy the other selection criteria), yielding small $\theta_{\rm SoI}$. To successfully cross-check the maser and cold molecular dynamics methods, maser-hosting galaxies that are both nearby and have regular dust/molecular gas distributions are required.

5 LINKS BETWEEN DISC PROPERTIES AND MASER EMISSION

The current ALMA observations can help uncover the relationship between the (central) molecular gas discs and masers. For example, all three galaxies studied here have a somewhat disturbed and/or clumpy molecular gas disc with a central mass concentration and likely non-circular motions.

To improve the number statistics and probe these trends further, we searched the literature for other published CO interferometric observations (i.e. moment maps) of galaxies in our parent sample of maser-hosting galaxies (Table 1). In addition to the aforementioned NGC 1386 and Circinus in Section 2.1 (and the three galaxies presented in this paper), there are publications concerning the galaxies NGC 1068, NGC 2273, NGC 4388, and NGC 4945. All except NGC 2273 show features similar to those of the three galaxies presented in this paper. The CO (2–1) molecular gas in NGC 1386 has regular rotation on large scales (within $\approx$1 kpc in radius) but the centre ($\approx$220 pc in radius) is kinematically decoupled at a spatial resolution of 36 pc, leading to significant residuals from axisymmetric models (Ramakrishnan et al. 2019). Other kinematic kinks caused by the bar can also be seen in the CO (1–0) data presented by Zabel et al. (2019). These features resemble those of NGC 5765B. The molecular gas in the Circinus Galaxy consists of nuclear spiral arms (within $\approx$40 pc in radius) and a circumnuclear disc ($\approx$10 pc in radius), the latter showing a highly distorted velocity field at a spatial resolution of 3 pc (Izumi et al. 2018; Tristram et al. 2022). NGC 1068 has a ring-shaped deficit of molecular gas ($\approx$130 pc outer diameter) surrounding a CO-rich nucleus, and it shows strong distortions (at a resolution of 6 pc) in its velocity field both outside (i.e. beyond a radius of

≈200 pc) and within (i.e. within a radius of ≈15 pc) the ring-shaped deficit, presumably caused by AGN outflows (García-Burillo et al. 2019). The CO (2–1) kinematics in the central ≈500 pc in radius of NGC 2273 is almost perfectly regular at a spatial resolution of $90 \times 72\,\mathrm{pc}^2$, although the CO (2–1) distribution is similar to that of NGC 5765B, showing evidence of a molecular gas-rich nuclear spiral (Domínguez-Fernández et al. 2020). NGC 4388 has a molecular gas depression in the central ≈20 pc in radius as well as prominent kpc-scale molecular gas outflows, the latter causing significant kinematic disturbances (at 12-pc resolution) in the nucleus (i.e. within a radius of ≈40 pc; Domínguez-Fernández et al. 2020; García-Burillo et al. 2021). In NGC 4945, prominent outflows and bar-driven inflows of molecular gas are traced by CO (3–2) (Bolatto et al. 2021) and multiple dense-gas tracers (Henkel et al. 2018). The gas kinematics is highly disturbed within a radius of ≈250 pc at a resolution of 40 pc (see e.g. fig. 8 of Henkel et al. 2018), although a nuclear disc of ≈50 pc radius may be regularly rotating (see e.g. fig. 12 of Henkel et al. 2018).

Of the nine maser galaxies with spatially resolved CO observations discussed above, almost all have morphological irregularities and/or kinematic disturbances and/or inflows/outflows, the only exception being NGC 2273 (that nevertheless shows potential bar-driven gas inflows). Although this sample is neither fully representative nor sufficiently large, the observations do suggest an emerging correlation between the properties of the central molecular gas disc and the existence of masers. It may be that a disturbed gas disc and/or gas inflows at kiloparsec scale is necessary to form a very dense molecular gas concentration at parsec scale, in turn triggering maser emission. Alternatively, it may be that AGN with masers are likely to cause irregularities in the gas discs, potentially through interactions between jets and the ISM.

As masers mostly reside in Seyfert 2 AGN, to understand whether this emerging trend is exclusive to maser galaxies or is more generally associated with the whole Seyfert 2 galaxy population, we searched the literature for other (non-maser-hosting) Seyfert 2 galaxies with published interferometric observations of cold molecular gas. Stuber et al. (2021) reported a frequency of 53 per cent of outflows in a sample of 19 AGN (mainly type 2), as part of the Physics at High Angular resolution in Nearby Galaxies (PHANGS) project. However, they did not discuss other non-circular motions. Alonso-Herrero et al. (2020) presented the zeroth-moment maps of 18 Seyfert galaxies (including 10 Seyfert 2) in their fig. 1. The sample was selected to have published mid-infrared spectral observations. All these galaxies have some morphological irregularities, such as non-axisymmetric gas distributions, off-centred peaks, holes/gaps and/or nuclear rings/spirals. This suggests that molecular gas irregularities are prevalent in the entire Seyfert 2 population. Nevertheless, the sample is still small in size, with unexplored potential biases, and critically the cold gas kinematics has not yet been explored.

Among publications with velocity maps available, all (non-maser-hosting) Seyfert 2 galaxies have features similar to those described in this work, e.g. Mrk 1066, NGC 7465 (Domínguez-Fernández et al. 2020), NGC 4968, and NGC 4845 (Bewketu Belete et al. 2021). However, the samples are even smaller in size and/or do not aim to be representative of all Seyfert 2 galaxies. Most publications concern a single object and aim to report non-circular motions in the first place.

Therefore, it is difficult to draw any statistical conclusion about how prevalent irregular kinematic features are in (non-maser-hosting) Seyfert 2 galaxies, to contrast with the maser sample discussed in this section. In addition, the non-detection of masers in Seyfert 2 galaxies may well be due to inclination effects rather than the non-existence of masers. Thus, physical differences between maser-hosting and non-maser-hosting Seyfert 2 galaxies will be difficult to establish without large and carefully-constructed samples of both.

All in all, while the above discussion is inconclusive, further investigation of the trend reported is warranted and desirable.

6 SUMMARY AND CONCLUSIONS

Our primary goal was to identify galaxies with existing megamaser SMBH mass measurements that are also promising targets for future measurements using high-angular-resolution (∼0.″01) ALMA molecular-gas observations, to cross-check the two methods. Considering all galaxies with a megamaser SMBH mass measurement, three promising galaxies were identified (NGC 1194, NGC 3393 and NGC 5765B) and new ALMA intermediate angular resolution (≈0.″5) and JCMT single-dish observations were obtained. The main results are as follows.

(i) NGC 1194 has an edge-on, disturbed and lopsided central CO (2–1) distribution dominated by two large components that appear associated with an irregular dust lane crossing the galaxy centre. The 230-GHz continuum emission is dominated by a single compact nuclear source.

(ii) NGC 3393 has fairly regular but patchy CO (2–1) emission, with little gas near the kinematic major axis and only faint diffuse emission in the very centre. There are also two brighter structures in the central region that are reminiscent of (part of) a nuclear ring and/or spiral. The velocity field has kinematic twists typical of (doubly) barred disc galaxies. The 230-GHz continuum emission is dominated by two compact sources. Combined with radio continuum flux densities from the literature, these reveal spectral indices typical of AGN/jets.

(iii) NGC 5765B has very bright CO (2–1) emission exhibiting the typical morphology and dynamics of a barred disc galaxy, with emission concentrated along two bisymmetric offset dust lanes (probably tracing shocks) and two bisymmetric nuclear spiral arms, with associated kinematic twists in the velocity field and large line-widths probably due to the shocks. The 230-GHz continuum emission is dominatedby a compact nuclear source and extended diffuse emission on one side of the nucleus.

Overall, partially because of the disturbed molecular gas kinematics, but primarily because of the extremely long observation times required, none of the three galaxies is promising for a future SMBH mass measurement using molecular gas. These difficulties directly arise from the properties of maser-hosting galaxies: (i) frequent co-existence of masers and disturbed CO kinematics, as discussed in Section 5; (ii) relatively low SMBH masses ($\sim 10^7\,\mathrm{M}_\odot$), yielding small R_{SoI}; and (iii) scarcity of masers, yielding typically large galaxy distances and thus small θ_{SoI}.

Apart from our three target galaxies, other candidates could emerge if the parent sample of maser-hosting galaxies were enlarged and/or the selection criteria used in this paper were moderately relaxed. In particular, by observing (different molecular lines) at higher frequencies, the criterion of resolving the putative SMBH SoI with a 0.″01 synthesized beam could be relaxed (although the observing times required are likely to remain impractically long). In practice, the order-of-magnitude estimate of a SMBH SoI adopted in this paper (see Section 2.1) is also often smaller than actual measurements (e.g. Yoon 2017).

None the less, the new CO observations presented in this paper have significantly added to the rather small number of spatially-resolved molecular gas studies of maser-hosting galaxies. A detailed

morphological and kinematical examination of our three targets, as well as six other maser-hosting galaxies with analogous observations from the literature, has revealed a potential correlation between molecular gas disturbances and/or inflows/outflows and the existence of maser emission.

ACKNOWLEDGEMENTS

We thank the anonymous referee for the helpful comments. MDS acknowledges support from a Science and Technology Facilities Council (STFC) DPhil studentship ST/N504233/1. MB was supported by STFC consolidated grant 'Astrophysics at Oxford' ST/K00106X/1 and ST/W000903/1. TAD acknowledges support from a STFC Ernest Rutherford Fellowship. This paper used the following ALMA data: ADS/JAO.ALMA#2015.1.00086.S and ADS/JAO.ALMA#2016.1.01553.S. ALMA is a partnership of ESO (representing its member states), NSF (USA), and NINS (Japan), together with NRC (Canada), MOST and ASIAA (Taiwan), and KASI (Republic of Korea), in cooperation with the Republic of Chile. The Joint ALMA Observatory is operated by ESO, AUI/NRAO and NAOJ. The James Clerk Maxwell Telescope is operated by the East Asian Observatory on behalf of The National Astronomical Observatory of Japan, Academia Sinica Institute of Astronomy and Astrophysics, Korea Astronomy and Space Science Institute, National Astronomical Research Institute of Thailand, Center for Astronomical Mega-Science (as well as the National Key R&D Program of China No. 2017YFA0402700). Additional funding support is provided by the Science and Technology Facilities Council of the United Kingdom and participating universities and organizations in the United Kingdom and Canada. The Starlink software (Currie et al. 2014) is currently supported by the East Asian Observatory. This research used observations made with the NASA/ESA *Hubble Space Telescope* and obtained from the Hubble Legacy Archive, which is a collaboration between the Space Telescope Science Institute (STScI/NASA), the Space Telescope European Coordinating Facility (ST-ECF/ESA), and the Canadian Astronomy Data Centre (CADC/NRC/CSA). This research also used the NASA/IPAC Extragalactic Database (NED), which is operated by the Jet Propulsion Laboratory, California Institute of Technology, under contract with the National Aeronautics and Space Administration, NASA's Astrophysics Data System Bibliographic Services and Cube Analysis and Rendering Tool for Astronomy (CARTA) for data visualization and measurements (Comrie et al. 2021). The Digitized Sky Surveys were produced at the Space Telescope Science Institute under U.S. Government grant NAG W-2166. Funding for the SDSS and SDSS-II has been provided by the Alfred P. Sloan Foundation, the Participating Institutions, the National Science Foundation, the U.S. Department of Energy, the National Aeronautics and Space Administration, the Japanese Monbukagakusho, the Max Planck Society, and the Higher Education Funding Council for England. The SDSS Web Site is http://www.sdss.org/. The SDSS is managed by the Astrophysical Research Consortium for the Participating Institutions. The Participating Institutions are the American Museum of Natural History, Astrophysical Institute Potsdam, University of Basel, University of Cambridge, Case Western Reserve University, University of Chicago, Drexel University, Fermilab, the Institute for Advanced Study, the Japan Participation Group, Johns Hopkins University, the Joint Institute for Nuclear Astrophysics, the Kavli Institute for Particle Astrophysics and Cosmology, the Korean Scientist Group, the Chinese Academy of Sciences (LAMOST), Los Alamos National Laboratory, the Max-Planck-Institute for Astronomy (MPIA), the Max-Planck-Institute for Astrophysics (MPA), New Mexico State University, Ohio State University, University of Pittsburgh, University of Portsmouth, Princeton University, the United States Naval Observatory and the University of Washington.

DATA AVAILABILITY

The raw ALMA data and the JCMT data obtained for this paper are available to download at the ALMA archive (https://almascience.nrao.edu/asax/) and the JCMT Science Archive (https://www.eaobservatory.org/jcmt/science/archive/), respectively. The *HST* images are available at the Hubble Legacy Archive (https://hla.stsci.edu/hlaview.html#). The final data products and original plots generated for the research underlying this article will be shared upon reasonable requests to the first author.

REFERENCES

Adelman-McCarthy J. K. et al., 2008, ApJS, 175, 297
Albareti F. D. et al., 2017, ApJS, 233, 25
Alexander D. M., Hickox R. C., 2012, New A Rev., 56, 93
Alonso-Herrero A. et al., 2020, A&A, 639, A43
Athanassoula E., 1992, MNRAS, 259, 345
Athanassoula E., Beaton R. L., 2006, MNRAS, 370, 1499
Barth A. J., Boizelle B. D., Darling J., Baker A. J., Buote D. A., Ho L. C., Walsh J. L., 2016, ApJ, 822, L28
Baumgartner W. H., Tueller J., Markwardt C. B., Skinner G. K., Barthelmy S., Mushotzky R. F., Evans P. A., Gehrels N., 2013, ApJS, 207, 19
Beifiori A., Courteau S., Corsini E. M., Zhu Y., 2012, MNRAS, 419, 2497
Bewketu Belete A. et al., 2021, A&A, 654, A24
Boizelle B. D., Barth A. J., Walsh J. L., Buote D. A., Baker A. J., Darling J., Ho L. C., 2019, ApJ, 881, 10
Boizelle B. D. et al., 2021, ApJ, 908, 19
Bolatto A. D., Wolfire M., Leroy A. K., 2013, ARA&A, 51, 207
Bolatto A. D. et al., 2021, ApJ, 923, 83
Braatz J. A., Condon J. J., Henkel C., Lo K. Y., Reid M. J., 2009, in astro2010: The Astronomy and Astrophysics Decadal Survey. p. 23
Broderick A. E. et al., 2022, ApJ, 935, 61
CASA Team et al., 2022, PASP, 134, 114501
Cappellari M., Verolme E. K., van der Marel R. P., Verdoes Kleijn G. A., Illingworth G. D., Franx M., Carollo C. M., de Zeeuw P. T., 2002, ApJ, 578, 787
Cappellari M., Neumayer N., Reunanen J., van der Werf P. P., de Zeeuw P. T., Rix H. W., 2009, MNRAS, 394, 660
Choi W. et al., 2023, MNRAS, 522, 4078
Cohn J. H. et al., 2021, ApJ, 919, 77
Comrie A. et al., 2021, CARTA: Cube Analysis and Rendering Tool for Astronomy, Astrophysics Source Code Library, record ascl:2103.031
Cooke A. J., Baldwin J. A., Ferland G. J., Netzer H., Wilson A. S., 2000, ApJS, 129, 517
Cornwell T. J., 2008, IEEE Journal of Selected Topics in Signal Processing, 2, 793
Currie M. J., Berry D. S., Jenness T., Gibb A. G., Bell G. S., Draper P. W., 2014, in Manset N., Forshay P., eds, ASP Conf. Ser. Vol. 485, Astronomical Data Analysis Software and Systems XXIII, Astron. Soc. Pac., San Francisco, p. 391
D'Onofrio M., Marziani P., Chiosi C., 2021, Front. Astron. Space Sci., 8, 157
Davies R. I. et al., 2006, ApJ, 646, 754
Davis T. A., Bureau M., Cappellari M., Sarzi M., Blitz L., 2013, Nature, 494, 328
Davis T. A., Bureau M., Onishi K., Cappellari M., Iguchi S., Sarzi M., 2017, MNRAS, 468, 4675
Davis T. A. et al., 2018, MNRAS, 473, 3818
Davis T. A. et al., 2020, MNRAS, 496, 4061
Davis T. A. et al., 2022, MNRAS, 512, 1522

de Vaucouleurs G., de Vaucouleurs A., Corwin H. G., Jr, Buta R. J., Paturel G., Fouque P., 1991, in Third Reference Catalogue of Bright Galaxies. Springer, New York
Devereux N., Ford H., Tsvetanov Z., Jacoby G., 2003, AJ, 125, 1226
Domínguez-Fernández A. J. et al., 2020, A&A, 643, A127
Drehmer D. A., Storchi-Bergmann T., Ferrari F., Cappellari M., Riffel R. A., 2015, MNRAS, 450, 128
Event Horizon Telescope Collaboration et al., 2019, ApJ, 875, L6
Fabbiano G., Wang J., Elvis M., Risaliti G., 2011, Nature, 477, 431
Feldmeier-Krause A., Zhu L., Neumayer N., van de Ven G., de Zeeuw P. T., Schödel R., 2017, MNRAS, 466, 4040
Ferrarese L., Merritt D., 2000, ApJ, 539, L9
Finlez C., Nagar N. M., Storchi-Bergmann T., Schnorr-Müller A., Riffel R. A., Lena D., Mundell C. G., Elvis M. S., 2018, MNRAS, 479, 3892
Gao F. et al., 2016, ApJ, 817, 128
Gao F. et al., 2017, ApJ, 834, 52
García-Burillo S. et al., 2019, A&A, 632, A61
García-Burillo S. et al., 2021, A&A, 652, A98
Gebhardt K., Thomas J., 2009, ApJ, 700, 1690
Gebhardt K. et al., 2000, ApJ, 539, L13
Gebhardt K., Adams J., Richstone D., Lauer T. R., Faber S. M., Gültekin K., Murphy J., Tremaine S., 2011, ApJ, 729, 119
Greene J. E., Seth A., Lyubenova M., Walsh J., van de Ven G., Läsker R., 2014, ApJ, 788, 145
Greene J. E. et al., 2016, ApJ, 826, L32
Greenhill L. J., Moran J. M., Herrnstein J. R., 1997, ApJ, 481, L23
Greenhill L. J. et al., 2003, ApJ, 590, 162
Greenhill L. J., Tilak A., Madejski G., 2008, ApJ, 686, L13
Haynes M. P. et al., 2018, ApJ, 861, 49
Henkel C. et al., 2018, A&A, 615, A155
Herrnstein J. R., Moran J. M., Greenhill L. J., Trotter A. S., 2005, ApJ, 629, 719
Hicks E. K. S., Malkan M. A., 2008, ApJS, 174, 31
Hovatta T. et al., 2014, AJ, 147, 143
Huré J. M., Hersant F., Surville C., Nakai N., Jacq T., 2011, A&A, 530, A145
Imanishi M., Saito Y., 2014, ApJ, 780, 106
Izumi T., Wada K., Fukushige R., Hamamura S., Kohno K., 2018, ApJ, 867, 48
Jenness T., Economou F., 2015, Astron. Comput., 9, 40
Jeter B., Broderick A. E., 2021, ApJ, 908, 139
Jeter B., Broderick A. E., McNamara B. R., 2019, ApJ, 882, 82
Kabasares K. M. et al., 2022, ApJ, 934, 162
Karachentsev I. D., Makarov D. A., 1996, AJ, 111, 794
Kim W.-T., Stone J. M., 2012, ApJ, 751, 124
Komatsu E. et al., 2009, ApJS, 180, 330
Kondratko P. T. et al., 2006, ApJ, 638, 100
Kondratko P. T., Greenhill L. J., Moran J. M., 2008, ApJ, 678, 87
Kormendy J., Ho L. C., 2013, ARA&A, 51, 511
Koss M. J. et al., 2015, ApJ, 807, 149
Koss M. J. et al., 2021, ApJS, 252, 29
Krajnović D., Cappellari M., de Zeeuw P. T., Copin Y., 2006, MNRAS, 366, 787
Kuo C. Y. et al., 2011, ApJ, 727, 20
Kuo C. Y., Braatz J. A., Reid M. J., Lo K. Y., Condon J. J., Impellizzeri C. M. V., Henkel C., 2013, ApJ, 767, 155
Kuo C. Y. et al., 2015, ApJ, 800, 26
Läsker R., Greene J. E., Seth A., van de Ven G., Braatz J. A., Henkel C., Lo K. Y., 2016, ApJ, 825, 3
Lelli F., Davis T. A., Bureau M., Cappellari M., Liu L., Ruffa I., Smith M. D., Williams T. G., 2022, MNRAS, 516, 4066
Liepold E. R., Ma C.-P., Walsh J. L., 2023, ApJ, 945, L35
Lodato G., Bertin G., 2003, A&A, 398, 517
Lu A. et al., 2022, MNRAS, 514, 5035
Mukherjee D., Wagner A. Y., Bicknell G. V., Morganti R., Oosterloo T., Nesvadba N., Sutherland R. S., 2018a, MNRAS, 476, 80
Mukherjee D., Bicknell G. V., Wagner A. Y., Sutherland R. S., Silk J., 2018b, MNRAS, 479, 5544
Nagai H. et al., 2019, ApJ, 883, 193
Nair P. B., Abraham R. G., 2010, ApJS, 186, 427
Neumayer N., Cappellari M., Reunanen J., Rix H. W., van der Werf P. P., de Zeeuw P. T., Davies R. I., 2007, ApJ, 671, 1329
Nguyen D. D. et al., 2020, ApJ, 892, 68
Nguyen D. D. et al., 2021, MNRAS, 504, 4123
Nguyen D. D. et al., 2022, MNRAS, 509, 2920
North E. V. et al., 2019, MNRAS, 490, 319
Oh K. et al., 2018, ApJS, 235, 4
Onishi K., Iguchi S., Sheth K., Kohno K., 2015, ApJ, 806, 39
Onishi K., Iguchi S., Davis T. A., Bureau M., Cappellari M., Sarzi M., Blitz L., 2017, MNRAS, 468, 4663
Onken C. A. et al., 2007, ApJ, 670, 105
Pastorini G. et al., 2007, A&A, 469, 405
Pesce D. W., Braatz J. A., Condon J. J., Gao F., Henkel C., Litzinger E., Lo K. Y., Reid M. J., 2015, ApJ, 810, 65
Pesce D. W. et al., 2020, ApJ, 891, L1
Pjanka P., Greene J. E., Seth A. C., Braatz J. A., Henkel C., Lo F. K. Y., Läsker R., 2017, ApJ, 844, 165
Ramakrishnan V. et al., 2019, MNRAS, 487, 444
Reid M. J., Braatz J. A., Condon J. J., Lo K. Y., Kuo C. Y., Impellizzeri C. M. V., Henkel C., 2013, ApJ, 767, 154
Reynolds T. N. et al., 2022, MNRAS, 510, 1716
Ruffa I. et al., 2019a, MNRAS, 484, 4239
Ruffa I. et al., 2019b, MNRAS, 489, 3739
Ruffa I., Prandoni I., Davis T. A., Laing R. A., Paladino R., Casasola V., Parma P., Bureau M., 2022, MNRAS, 510, 4485
Ruffa I. et al., 2023, MNRAS, 522, 6170
Saglia R. P. et al., 2016, ApJ, 818, 47
Schmitt H. R., Donley J. L., Antonucci R. R. J., Hutchings J. B., Kinney A. L., 2003, ApJS, 148, 327
Shapiro K. L., Cappellari M., de Zeeuw T., McDermid R. M., Gebhardt K., van den Bosch R. C. E., Statler T. S., 2006, MNRAS, 370, 559
Shirazi M., Brinchmann J., 2012, MNRAS, 421, 1043
Simon D. A., Cappellari M., Hartke J., 2024, MNRAS, 527, 2341
Siopis C. et al., 2009, ApJ, 693, 946
Skrutskie M. F. et al., 2006, AJ, 131, 1163
Smith M. D. et al., 2019, MNRAS, 485, 4359
Smith M. D. et al., 2021, MNRAS, 503, 5984
Stuber S. K. et al., 2021, A&A, 653, A172
Sun A.-L., Greene J. E., Impellizzeri C. M. V., Kuo C.-Y., Braatz J. A., Tuttle S., 2013, ApJ, 778, 47
Toba Y. et al., 2014, ApJ, 788, 45
Tristram K. R. W. et al., 2022, A&A, 664, A142
van den Bosch R. C. E., 2016, ApJ, 831, 134
van den Bosch R. C. E., Greene J. E., Braatz J. A., Constantin A., Kuo C.-Y., 2016, ApJ, 819, 11
van der Walt S. et al., 2014, PeerJ, 2, e453
Verdoes Kleijn G. A., van der Marel R. P., de Zeeuw P. T., Noel-Storr J., Baum S. A., 2002, AJ, 124, 2524
Walsh J. L., van den Bosch R. C. E., Barth A. J., Sarzi M., 2012, ApJ, 753, 79
Walsh J. L., Barth A. J., Ho L. C., Sarzi M., 2013, ApJ, 770, 86
Yamauchi A., Nakai N., Sato N., Diamond P., 2004, PASJ, 56, 605
Yamauchi A., Nakai N., Ishihara Y., Diamond P., Sato N., 2012, PASJ, 64, 103
Yoon I., 2017, MNRAS, 466, 1987
Young L. M. et al., 2011, MNRAS, 414, 940
Zabel N. et al., 2019, MNRAS, 483, 2251
Zhao W. et al., 2018, ApJ, 854, 124

This paper has been typeset from a TEX/LATEX file prepared by the author.